*Small*

NANO · MICRO small
www.small-journal.com

RESEARCH ARTICLE

# Synergistic Charge Redistribution in a Dual-Atomic Fe−$CoN_6$ on Nanofiber With Fe−N Site Preference of Intermediates Compared to Pristine Fe Single Atoms for Oxygen Redox in Zinc-Air Battery

Anubha Yadav[1] | Antra Mohini[2,3] | Babasaheb M. Matsagar[4,5] | Norman C.-R. Chen[4,6] | Ahin Roy[7] | Kevin C.-W. Wu[4,8,9,10] | Amreen Bano[2,3] | Saikat Dutta[1]

[1]Electrochemical Energy & Sensor Research Laboratory, Amity Institute of Click Chemistry Research & Studies, Amity University, Noida, India | [2]Research Institute for Sustainable Energy, Centres For Research and Education in Science and Technology (TCG-CREST), Kolkata, India | [3]Academy of Scientific and Innovative Research (AcSIR), Ghaziabad, India | [4]Department of Chemical Engineering, National Taiwan University, Taipei, Taiwan | [5]Graduate School of Biotechnology and Bioengineering, Yuan Ze University, Taoyuan, Taiwan | [6]Molecular Science and Technology Program, Taiwan International Graduate Program, Academia Sinica, Taipei, Taiwan | [7]Materials Science Centre, Indian Institute of Technology Kharagpur, Kharagpur, West Bengal, India | [8]Department of Chemical Engineering and Materials Science, Yuan Ze University, Taoyuan, Taiwan | [9]Department of Applied Chemistry, Graduate School of Engineering, Tohoku University, Sendai, Miyagi, Japan | [10]Department of Chemical Engineering, Faculty of Engineering, Chulalongkorn University, Bangkok, Thailand

**Correspondence:** Amreen Bano (amreen.bano@tcgcrest.org) | Saikat Dutta (sdutta2@amity.edu)

**Received:** 22 January 2026 | **Revised:** 21 May 2026 | **Accepted:** 9 June 2026

**Keywords:** DOS of $FeCoN_6$ | electron conduction | Fe−Co bridging dual-atom | Fe−N-preferred $O_2$ adsorption | synergistic charge redistribution

## ABSTRACT

Reducing the reaction barriers of the oxygen reduction reaction (ORR) and accelerating the reaction kinetics of zinc-air batteries (ZABs) requires unique advantages in regulating electron orbitals with weakened adsorption of oxygen intermediates and conductive dissociation with a negative shift of the *d-band* center. The sluggish ORR and unstable Zn/electrolyte interface at relatively high-rate ability require bifunctional electrolysis. Herein, a multi-walled carbon nanotube (MWCNT) and resorcinol-formaldehyde (RF) polymer composite resulted nanofiber in which Fe and Co-atomic sites were incorporated in $Fe_A$-$Co_A$/MWCNT-NC. As compared between the bridging Fe−Co and lateral Fe−Co model by Density Functional Theory (DFT) simulation and Bader charge analysis, optimal charge transfer at bridging with faster ORR kinetics as a result of balanced adsorption energy and electron distribution suggests a Fe−Co bridging model is more active. A comparison of ORR and ZAB with single-atomic FeSA950NC supports the DFT results of charge distribution and weakened adsorption of ORR intermediates. ORR and ZAB results reveal: 1) bridging atom sites with moderate charge polarization due to delocalization of *d-band* electrons, 2) significant electron conduction, 3) more adsorption-desorption on Fe−N sites. These findings offer insights into the electron redistribution in sites of electrodes and rational design for high-performance electrodes in energy storage devices.

Anubha Yadav and Antra Mohini contributed equally to this work.

## 1 | Introduction

Dual-atomic site containing electrodes offer a synergism between constituent elements on a graphenic matrix are capable of modulating the multiple reaction intermediates via regulating electron orbitals with negative shifts of the *d-band* center [1]. Single-atom materials exhibit distinct atomic structures and electrical characteristics that are different from their nanoparticulate. The synergistic interactions between metal atoms and the coordinating atoms have a vital role in altering the electronic characteristics of the metal active sites, therefore regulating the electrochemical processes [2, 3]. Diatomic-sites naturally inherit the alteration of electron distribution around metal atoms as compared with isolated single-atoms via the utilization of two adjacent metal atomic species to achieve synergistic effects in which negative shifts of *d-band* center, more conductive to the dissociation of oxygen intermediates, and optimized reaction kinetics have built the foundation for improving the performance of zinc-air batteries (ZABs) [4]. Generally, orbital coupling from two adjacent metal atoms ($d_{xy}$ and $d_{xz}$ orbitals) decreases the orbital energy levels for weakening the bond strength of intermediate species [5]. The single-atom-dimer (SAD) can buffer the multiple reaction intermediates with a strategy to modify the electronic structure and environment around the synergistic metal atoms bridged by one oxygen [6, 7]. Pd−O−Cu bridged dimer-site facilitates the photoelectron transfer to the active site for inhibiting the recombination, for balancing adsorption-desorption in photo $H_2$ evolution [8]. Regulation of electrons in single-atom $CoN_4$ to $Co_2N_5$ dual atoms by using an atomization and sintering strategy via an N-stripping and thermal migration process, including a tailored spin-state, could achieve balanced adsorption/desorption of intermediates [9]. Therefore, thermal migration forming paired single-atom $CoN_4$ into a dimer $Co_2N_5$ was confirmed from X-ray absorption spectral contour analysis [9]. In situ trapping of Ni and Co ions in molybdenum polydopamine nanosheet, followed by annealing with precise tuning of the nitrogen moieties as ultrathin Ni−Co single-atom dimer [10]. Randomly anchored Pt and Ru single atoms on a g-$C_3N_4$ result from Pt-Ru dimers depending on the orbital coupling of neighboring atoms [5]. Programmable phthalocyanine dimer on N-doped graphitic carbon by delocalized dispersion during pyrolysis results in excellent ORR and zinc-air battery performance, wherein a synergistic interaction balances the d-band center and free energy O* intermediates [11]. Such a dimeric atomic interface is electrochemically different from the bimetallic nanoclusters comparable to single-atom nanozymes [12]. In this context, the controlled formation of dimer atom Au-Ru on activated carbon and spatially isolated single-atom on NC, which exhibits distinct signatures of HER based on two of their different architectures, emphasizes the relevance of intermetallic coordination for optimally structured atom dimers [13]. Due to the interaction between dual-atom sites, including precise adjustment of dual-atom coordination sites, inheritance of single-atom materials in the dimeric-diatom system was not perfectly carried including identification of diatom sites and challenges in structural stability [14]. Bimetallic dimer structure as dual atom dimers via atomic layer deposition offer improved stability and higher mass activity with Pt−Ru−N structural unit [15]. These kinds of diatom dimers is distinctly from the surface d charge of bimetallic alloy e. g. AuPd [16, 17].

Owing to promising ORR by dual-atom sites in air-cathode, bottleneck of durability by oxidative by-products is a major hurdle. The precise modulation of local electronic environment is another challenge for weakening *OH adsorption as rate limiting step of ORR with maximized peak power density for longer hours [18]. Therefore, the durability of the electrode and the desired electronic environment for intermediate adsorption remain the key bottlenecks for the ZABs. Fe, Zr-NC achieves a high half-wave potential (0.891 V) vs reversible hydrogen electrode (RHE)) with minimum activity loss over 5000 cycles along with peak power density of 185.7 $cm^{-2}$ for 453 h [19]. Dual Fe-Ni pair in FeNi−NHC offers a peak power density of 126 mW $cm^{-2}$ at 204 mA $cm^{-2}$, 1.45 times higher than that of its counterparts Fe−$N_4$ or Ni−$N_4$, along with a ZAB FeNi−NHC air-cathode with open-circuit voltage (1.49 V) than Pt/C−$RuO_2$ (1.46 V) [20]. Dual single-atomic sites in CoMn/NC activate the O—O bond for the 4$e^-$ ORR via a dissociative mechanism [21]. Fe/$CoN_x$-C cathode excels in liquid and quasi-solid ZABs with a peak power density of 134.97 mW $cm^{-2}$ by facilitating reversible ORR as the rate-determining step [22]. ORR/ZAB oxygen reduction kinetics also depend on the two-dimensional structural features of electrode [23–25]. Additionally, site-specific synergy of a heteronuclear environment of atomic sites alters *d*-band centers for pushing the ORR in alkaline and acidic medium with higher stability boundaries [26]. ORR kinetics and required electronic environment modulation by a Co-SA and Co-low nuclear cluster optimizes the adsorption/desorption strength of oxygenated intermediates on the atomic sites for lowering half-wave potential and overpotential [2, 3]. This eventually provides better durability as compared to a single-atom Fe−$N_4$ system, which motivates the next level of investigation on site-preferences and synergistic charge distribution in dual-atomic sites for ZABs as compared to single-atomic sites. However, beyond DFT analysis and shifts of *d*-band centers, the factors driving the charge-distribution and site-preference of intermediate adsorption for ZABs by a dual-atomic system are not fully revealed.

Herein, we report the introduction of Fe−Co dual-atomic sites in a MWCNT and resorcinol-formaldehyde (RF) polymer-derived matrix denoted as $Fe_A$-$Co_A$/MWCNT-NC with two adjacent Fe and Co atoms at the interface MWCNT-NC with a ribbon-like architecture. This was used as air cathodes for ORR-driven ZABs. Dual-atomically dispersed $Fe_A$-$Co_A$/MWCNT-NC promotes electron transfer in ORR to the active dual-atomic interface along the ribbon-like MWCNT-NC. In addition, the $Fe_A$-$Co_A$/MWCNT-NC possesses a specific surface area of 102 $m^2$ $g^{-1}$ in a microporous network with high pyridinic-N and isolated atomic sites of dual-atoms as intermediate adsorption sites. These characteristics offer novelty in promoting the $Fe_A$-$Co_A$ hetero-dual atomic sites for the ORR and extension to the ZABs as an air cathode. Thus, $Fe_A$-$Co_A$/MWCNT-NC exhibits an exceptional positive half-wave potential 0.783 V, with accelerated kinetics (53.3 mV $dec^{-1}$ Tafel slope), and excellent ORR stability for 10000 cycles as revealed from RRDE experiment. A home-made assembly of ZABs with 6.0 M KOH/0.2 M $Zn(AC)_2$ mixed solution as the electrolyte, the open circuit voltage of $Fe_A$-$Co_A$/MWCNT-NC-based ZAB is 1.522 V, very close to that of Pt/C (1.47 V) and with maximum power density 213 mW $cm^{-2}$. The aqueous ZAB cell with $Fe_A$-$Co_A$/MWCNT-NC cathode present voltage plateaus of ≈1.28 V, higher than that of Pt/C. When ZAB of $Fe_A$-$Co_A$/MWCNT-NC

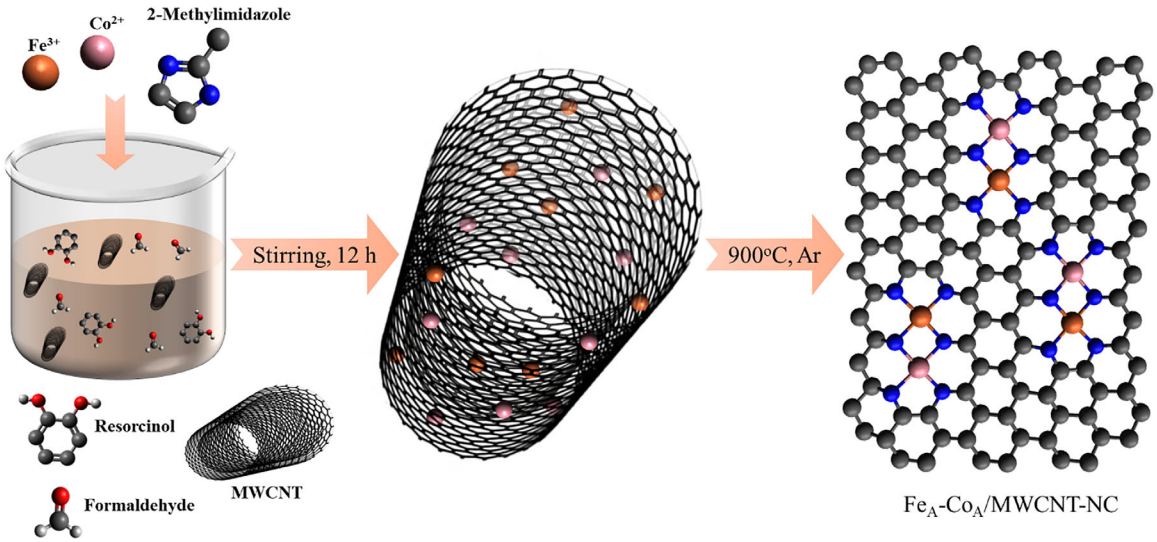


**FIGURE 1** | Schematic illustration of the synthetic strategy for the $Fe_A$-$Co_A$/MWCNT-NC involving 1) trapping of metal ions in 2-methylimidazole into resorcinol-formaldehyde in the presence of MWCNT under stirring for 12 h, 2) pyrolysis of the resulting composite at 900°C under argon for 2 h.

cathode was compared with a control sample $Fe_{SA}$950NC, the dual-atomic ieffect was substantial resulting from 1) the synergistic effect of dual-atom interfaces, 2) nano-ribbon-like structure of MWCNT-NC. $Fe_A$-$Co_A$/MWCNT-NC exhibits an exceptionally pH-universal ORR activity, requiring only 50.1 and 61 mV overpotential at −10 ms $cm^{-2}$ in acidic and alkaline media. Our DFT analysis reveals that Fe−Co dual-atom exhibits improved electronic cooperation due to 1) symmetric bridging, 2) favorable ORR intermediates adsorption, and 3) least charge-transfer strain. The dual-atomic bridging site enhances O−O activation and reduces ORR energy barriers, as confirmed by the combined PDOS and Bader-charge analyses by shared and optimal charge transfer. The symmetric bridging Fe−Co performs superior to the single-atom system and the lateral dual-atom configuration highlights the novelty and advancement in realizing electronics of dual-atoms. The FeSA950NC control sample used in this study was adopted from our previously reported work [27].

## 2 | Result and Discussion

Precisely, by controlling the amount of N, dual-atomic sites could be generated, with an optimum amount of N-moieties fused with MWCNT's structural feature, incorporated with heteronuclear dual-atom sites. Briefly, the synthetic strategy of $Fe_A$-$Co_A$/MWCNT-NC could be divided into two steps, as schematically illustrated in Figure 1. First, the targeted metal ions ($Fe^{+2}$ and $Co^{+2}$) were trapped in situ into a polymer resorcinol-formaldehyde (RF) and zeolitic imidazolate framework-8 (ZIF-8) composite, including MWCNT marked as $Fe^{+2}$-$Co^{+2}$@RF-MWCNT under continuous stirring. This was followed by the annealing of $Fe^{+2}$-$Co^{+2}$@RF-MWCNT at 900°C for 2 h in an argon atmosphere to result in a desired dual-atomic interface in $Fe_A$-$Co_A$/MWCNT-NC. The pyrolysis at 900°C led to the formation of MWCNT-NC with fiber-like networks, which resulted from the formation of a non-graphitic structure composed of randomly oriented curved and defective graphene nanosheets with a larger interlayer distance.

### 2.1 | Structural Analysis

The X-ray diffraction (XRD) pattern of the $Fe_A$-$Co_A$/MWCNT-NC exhibits graphitic carbon planes at (002) and (101) at 24° (sharp) and 43° (broad peak) 2$\theta$ correspond to the crystal planes of disordered graphite domains, respectively, which is typical of graphitic carbon (Figure 2a). Exhibiting a sharp peak at 24°, demonstrating that the graphite-like layers are highly stacked and the corresponding interlayer spacing is close to that of graphite. The pattern shows 24° diffraction peak assigned to (002) reflection of graphite [28]. This sharp peak confirms high graphitic crystalline characteristics of NC fused to MWCNT. Therefore, the possibility of forming Fe-Co alloy or Fe and Co purely metallic nanoparticles is excluded because of the use of a suitable proportion of 2-methylimidazone and resorcinol-formaldehyde polymer (RF) in forming a Fe-Co dual atomic interface with N-moieties in the $Fe^{+2}$-$Co^{+2}$@ZIF-8-RF. Therefore, dispersion of a dual metal atom site, along with carbon lattice defects was resulted in $Fe_A$-$Co_A$/MWCNT-NC. No peaks ascribed to Fe or Co nanoparticles were observed, confirming the high dispersion of dual atoms [29]. Raman spectra of $Fe_A$-$Co_A$/MWCNT-NC was obtained by using a spectrometer equipped with argon (532 nm) lasers, shows characteristics D and G band (Figure 2b) with $I_D/I_G$ 1.03, corresponds to defect concentration along with the graphene sheets and consistent with their corresponding XRD results [30]. To get an insight into the Brunauer–Emmett–Teller (BET) specific surface area (SSA) and pore size information, the $N_2$-adsorption-desorption isotherm was observed. Figure S1a displayed an SSA of 102.791 $m^2$ $g^{-1}$. The pore size distribution indicates that the Mn−$N_4$−N−CNF comprises meso- and micropores below 10 nm (Figure S1b).

X-ray absorption near-edge structure (XANES) and extended X-ray absorption fine structure (EXAFS) measurements were conducted to determine the chemical state and coordination environment of the Fe and Co atoms in $Fe_A$-$Co_AN_6$. These techniques, as shown in Fe and Co K-edge XANES spectra of $Fe_A$-$Co_A$/MWCNT-NC, along with Fe and Co metal foil as references,

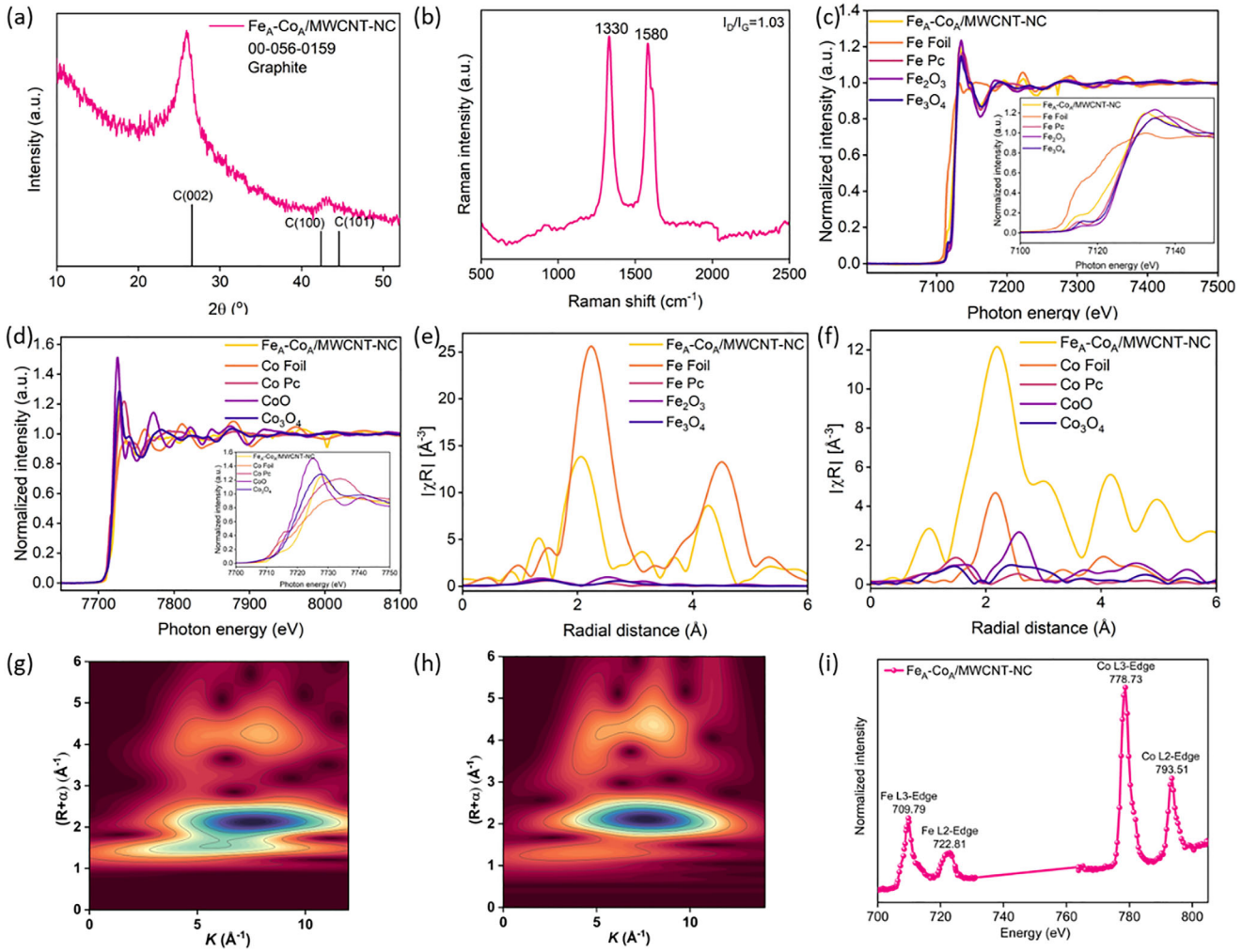


**FIGURE 2** | (a) XRD spectra of $Fe_A$-$Co_A$/MWCNT-NC. (b) Raman spectral plot of $Fe_A$-$Co_A$/MWCNT-NC recorded at 532 nm. Structural characterization by X-ray absorption spectroscopy. (c) Fe-K-edge EXAF spectra of $Fe_A$-$Co_A$/MWCNT-NC (The inset zoom in over the near edge feature). (d) Co-K-edge EXAF spectra (The inset zoom in over the near edge feature). (e) R-space Fe-K-edge spectra of $Fe_A$-$Co_A$/MWCNT-NC (f) R-space Fe-K-edge spectra of $Fe_A$-$Co_A$/MWCNT-NC. (g) WT-EXAFS of Fe-K-edge of $Fe_A$-$Co_A$/MWCNT-NC. (h) WT-EXAFS of Co-K-edge of $Fe_A$-$Co_A$/MWCNT-NC. (i) Soft-X-ray absorption spectra of L3-edge for $Fe_A$-$Co_A$/MWCNT-NC.

exhibited a characteristic pre-edge peak around 7114.023 eV in the Fe K-edge XANES spectra (Figure 2c) due to a 1s to 4pz shakedown transition of square-planar coordination with a $D_{4h}$ local symmetry [31]. The weak pre-edge peak intensity of $Fe_A$-$Co_A$/MWCNT-NC as compared to Fe-foil can be ascribed to the distorted D4h symmetry, indicating the coordination of the central Fe-atom with the nearest four N and adjacent metal atoms [32]. Such a distortion of $D_{4h}$ symmetry of the Fe-center resembles the weak pre-edge peak intensity of NiPC (PC = phthalocyanine) along with a possible higher oxidation state of $Fe_A$ in $Fe_A$-$Co_A$/MWCNT-NC, as found compared to FeSA-NC [33]. Similar pre-edge peak around 7712.21 eV for $Fe_A$-$Co_A$/MWCNT-NC in the Co K-edge profile (Figure 2d), suggesting the presence of X-ray absorbing Co-centers with N-coordination. Inset of Figure 2d shows the pre-edge feature to identify the electronic transition as compared to the Co-foil. As compared to the near-edge and white line features in the Co K-edge XANES profile of Ni-SA-NC and Ni-PC, a negative shift of the XANES profile at 7727.61 eV for $Fe_A$-$Co_A$/MWCNT-NC was observed (Figure 2d), which is comparable with that of the NiCo-SAD-NC atom dimer [33]. Figure S2a,b represent Fe and Co K-space K-edge spectra of $Fe_A$-$Co_A$/MWCNT-NC. Furthermore, Figure 2e,f displays the Fe and Co K-edge Fourier-transformed (FT) k3-weighted EXAFS spectra of $Fe_A$-$Co_A$/MWCNT-NC, with control samples Fe-foil and Co-foil. In the Fe K-edge FT-EXAFS spectra, the predominant peaks in the R-space at around (Figure 2e) 1.34 and 2.08 Å correspond to Fe—N bond and Fe−Co scattering path, respectively, as dual sites. Excluding the possibility of Fe—Fe bonding of metallic Fe as reference (2.23 Å), $Fe_A$-$Co_A$/MWCNT-NC contains a dual site with predominantly Fe−Co and Fe−$N_x$ path in which a major peak at 2.08 Å corroborates the formation of Fe−Co coordination, such cannot be found in pristine Fe−N−C single atom [34]. Similarly, in the Co K-edge FT-EXAFS spectra, the predominant peaks in the R-space at 2.23 Å correspond to a Co−Fe scattering path, along with a small peak at 1.56 Å corresponds to Co−N scattering path. A possible elongation from Co—N bond to 1.56 Å, as compared to Co−N SA sample, suggests a distortion resulting from $D_{4h}$ symmetry of Co atom center with the formation of an additional Fe—Co bond scattered at

2.23 Å, suggesting a Fe–Co dimer structure. In this context, hetero-atom dimer formation was confirmed by Co K-edge EXAFS R-space and fitting analysis for NiCo-SAD-NC wherein a Ni–Co scattering occurs at 2.40 Å [33]. Curve fitting analysis for the collected EXAFS data was performed to acquire quantitative local structural parameters for $Fe_A$-$Co_A$/MWCNT-NC. As illustrated in Figure S3 and Table S1, the Fe—N and Co—N bonding pairs in Fe and Co possess the coordination numbers of 4 (Table S1). It indicates that each isolated Fe atoms are bound by four N atoms while the neighboring Co atoms are found to be three Co/Fe atoms. These results confirm the formation of a composite architecture with Co–$N_4$ moieties and CoFeNCs. By contrast, EXAFS fitting results for $Fe_A$-$Co_A$/MWCNT-NC show that the Co atom adopts only the Co–$N_4$ structure. The detailed fitting parameters and results are shown in Table S1. After analysis and comparison, $Fe_A$-$Co_A$/MWCNT-NC has strong coordination absorption peaks of Fe–N, and Co–N. Generally, the synchrotron radiation plot line is not very accurate, especially since the distance will have an error of ≈0.5 Å. Therefore, an elaborate structure model fitting is employed for further quantitative analysis, and the accurate coordination number and atomic spacing. R-space Fe K-edge and Co K-edge FT-EXAFS spectra of FeA-CoA/MWCNT-NC showing characteristic Fe–Co scattering peaks at 2.05 and 2.20 Å, respectively. These peaks are absent in unsymmetric Fe–Co atom pairs but match the symmetric dimer scattering reported for NiCo-SAD-NC [33, 35].

The FT-EXAFS results were corroborated by the wavelet transform WT-EXAFS at the Fe K-edge (Figure 2g) and Co K-edge (Figure 2h). WT-EXAFS Fe K-edge shows a peak 7.47 K($Å^{-1}$) corresponding to Fe—Co bond, with a small contour extension to 3.66 K($Å^{-1}$) corresponding to Fe–N. This WT-contour of hetero-atom dimer of Fe–Co is significantly different from dual-atom materials, which consist of a Co—Co bond scattering to exhibit a contour at around 9 K($Å^{-1}$) [9]. Furthermore, WT-EXAFS Co K-edge shows a peak 7.79 K($Å^{-1}$) corresponding to Fe—Co bond with an additional contour peak at 4.36 K($Å^{-1}$) corresponding to Co–N as the secondary coordination sphere. To determine the detailed coordination structure of the Fe and Co atoms in $Fe_A$-$Co_A$/MWCNT-NC, fitted EXAFS at the Fe K-edge and Co K-edge were conducted. Soft X-ray L3-edge Co and Fe peaks in Figure 2i confirmed the presence of L3-edge and L2-edge peaks of both Fe and Co, which correspond to $Fe^{+3}$ and $Co^{+2}$ atom centers. L3-edge and L2-edge of Co correspond to L3 edge 778.7 eV and L2 edge at 793.5 eV, respectively.

Chemical bonding of metal-ions with the organic linker to ensure atomic dispersion followed by the encapsulation of second metal salts in the small ZIF-8 cavities results into Ni/Fe-N-C dual atom sites consisting of N-coordinated carbon and Ni–Fe coordination as metal-metal scattering path from EXAFS analysis [34]. In contrast, Ni and Co K-edge XANES spectra of NiCo-SAD-NC as reference samples showed a positive shift as compared to Ni-SA-NC, suggesting a higher oxidation state of Ni, and the opposite due to a negative shift for Co K-edge spectra, suggesting a lower oxidation state of Co with 4-coordination of N [33]. A distorted $D_{4h}$ local symmetry of Ni atom site with a Ni-metal peak at 2.18 Å, corroborating the formation of additional Ni–Co coordination along the Ni—N bonds, which is similar to the bonding of Zn–Co and Co–Fe dual sites [36]. Atomically scattered dual sites $CoN_4$/$FeN_4$ with adjacent nanocluster defects exhibit Co–N coordination shell at R ≈ 1.58 A, almost similar as in Co–N of CoPc. Least square curve fitting for the EXAFS data for quantitative local structural parameters for Co, Fe-DACs/NCs@PCF reveals coordination numbers of 3.79 and 2.66 respectively for Co—N and Co—Co/Fe bonding pairs with Co coordinating to four N atoms, while neighboring Co atoms are bound to three Co/Fe atoms resulting architecture of $CoN_4$ moieties [37]. Unsymmetrical Fe–Co diatomic pairs offer strong charge polarization between Co and Fe atoms. Spin-down electrons around Co atoms are much higher than those spin-up electrons, which results in a seesaw effect occurring between Co atoms and Fe atoms, resulting a negative shift of the d-band center. This means such a structural configuration of dual atoms in unsymmetrical mode weakens the adsorption of oxygen intermediates and is more conductive to their dissociation, which is reflected in peak power density 215 mW $cm^{-2}$ [35]. FeNi-DSAs-PNCH as air cathode in ZABs for a higher open-circuit voltage (1.48 V) with larger specific capacity results from abundant adjacent Ni–$N_x$ atomic sites, which modulate the d-band center of Fe–$N_x$ single atomic centers which balancing the adsorption-desorption affinities to $O_2$ and O-containing intermediates on Fe–$N_x$ [38]. EXAFS spectral analysis of $Fe_A$-$Co_A$/MWCNT-NC includes peaks at 1.34 and 2.08 Å corresponding to Fe–N and Fe–Co along with a possible elongation from Co—N bond to 1.56 Å. These suggest a strong Fe–Co coordination in which electronic balance during the ZAB and ORR performance is obvious which needs density functional theory (DFT) analysis for determining the electron flow of dual atomic sites.

It is found that attempts are made to closely compare and reveal the potentials and contributions of di-atomic and tri-atomic sites, including models of diatomic-triatomic comparison, along with a symmetric planner heterogeneous M–$N_4$ configuration of atoms on porous N-carbon for optimal utilization of robust performance for ZABs [39]. Based on the observation of EXAFS spectral peaks for Fe-K and Co-K R-space (Figure 2e,f) for $Fe_A$-$Co_A$/MWCNT-NC as compared to FeSA950NC [27] as cathodes in ZABs, peaks correspond to 1.31 Å (Fe–K) and 1.04 Å (Co–K) for Fe–N and Co–N, respectively, along with peaks at 2.05 Å (Fe-K) and 2.20 Å (Co-K), which correspond to Fe–Co scattering, unlike Fe and Co metal foils. Such dual-atom scattering of Fe–Co in $Fe_A$-$Co_A$/MWCNT-NC was likely similar to what was observed in the EXAFS spectral pattern of a Ni–Co dual atom in NiCo-SAD-NC, with a specific peak assigned to Ni–Co scattering for both Ni–K and Co–K EXAFS [33, 40]. However, in an unsymmetric arrangement of dual atoms Fe and Co, only peaks correspond to Fe–N and Co–N without any scattering peak for Fe–Co [35]. Therefore, EXAFS analysis of $Fe_A$-$Co_A$/MWCNT-NC suggests the possibility of a bridging structure of Fe–Co with X-ray scattering, which is unlikely in an unsymmetric dual atom Fe–N and Co–N sites. Our experimental results need theoretical support to demonstrate that the strong metal-carrier interaction interface supports the dynamic electron transfer between $FeN_x$ and $CoN_x$ units to enhance electronic conductivity and stability of the electrode. Strong metal-carrier interaction interface promotes dynamics of electron transfer between dual atomic sites, such as $CoFe_2O_4$ and Co atoms, by improved electronic conductivity and enhanced stability [41]. As in the case of carbon dots

(CDs), we have used nanofibrous architecture of MWCNT-NC for hosting dual atomic sites, wherein electron mobility from $Fe_{SA}$ to $Co_{SA}$ through the nanofibrous architecture would optimize the adsorption of O*/OH* and promote the release of the final product.

To further validate the symmetric bridging configuration of the Fe–$CoN_6$ sites, we compared our EXAFS results with literature precedents. In contrast to the unsymmetric Fe–Co diatomic pairs reported by Li et al., which exhibit no detectable Fe–Co scattering in either the Fe or Co K-edge R-space EXAFS and are therefore classified as non-dimeric atom pairs with a seesaw-type electronic effect [35], the $Fe_A$-$Co_A$/MWCNT-NC catalyst displays clear and intense Fe–Co scattering peaks at 2.05 Å (Fe K-edge) and 2.20 Å (Co K-edge) (Figure 2e,f). These features are analogous to the strong Ni–Co dimer scattering observed in the benchmark NiCo-SAD-NC system [33], confirming the presence of direct symmetric metal–metal interaction. Combined with the paired bright spots in AC-HAADF-STEM imaging (Figure 3e,f, blue circles) showing spatial overlap of Fe and Co at the atomic scale, these data provide compelling evidence for a bridging Fe–$CoN_6$ dimer geometry rather than isolated or purely lateral atom pairs.

Transmission electron microscopy (TEM) analysis (Figure 3a) reveals a nanofiber network of N-MWCNT-NC, a low-magnification bright-field image of the synthesized sample with the metal atoms. High resolution-TEM (HR-TEM) data of $Fe_A$-$Co_A$/MWCNT-NC (Figure 3b,c) reveal multi-walled carbon matrix with both randomly oriented graphite layer and uniformly long multi-walled structures as lattice planes of the MWCNT side walls are clearly visible. Moreover, the XRD of $Fe_A$-$Co_A$/MWCNT-NC exhibit two broad reflections at ≈26.2° and ≈43.3°, corresponding to the (002) and (101) planes of the graphite lattice, without any Co or Fe crystalline phase peaks [42]. Low magnification STEM image (Figure 3d) shows the network of MWCNT-NC with large particles too. HAADF-STEM image of $Fe_A$-$Co_A$/MWCNT-NC (Figure 3c) shows the white spots in dark-field mode, indicating Fe and Co atom density and uniform dispersion. HRTEM image of $Fe_A$-$Co_A$/MWCNT-NC (Figure 3d) reveals multi-walled fiber architecture. The BF-TEM and HRTEM depend on diffraction and phase contrast, respectively, making it difficult to discern single atoms. On the other hand, being devoid of any aberrations, aberration-corrected HAADF imaging in STEM mode can leverage the Z-contrast to discern the presence of Fe or Co atoms, as they have comparatively higher Z than C. Figure 3d shows a low magnification STEM of the sample, showing bright particles. Upon increasing the magnification, very bright contrast from atoms can be seen in Figure 3e, indicating the possible presence of Co and Fe. Aberration-corrected high-angle annular dark field-scanning transmission electron microscopy (AC-HAADF-STEM) (Figure 3e,f) demonstrates the uniform distribution of bright spots corresponding to Fe/Co single-atoms on MWCNT-NC marked with blue circles for atoms/dual-atoms and red circles for multi-atoms in Figure 3f. By contrast, the HAADF-STEM and EDS elemental mapping analysis for $Fe_A$-$Co_A$/MWCNT-NC demonstrate a uniform distribution of C, Co, and Fe across the MWCNT-NC, with no evidence of Fe NCs or NPs. Figure 3g shows the electron image of $Fe_A$-$Co_A$/MWCNT-NC with elemental mapping images corresponding to C-K, N-K, O-K, Co-K, and Fe-K edges. The overlay of the electron map (Figure 3g) with yellow yellow-marked arrow shows the overlay of Fe and Co atoms, revealing the possible presence of Fe-Co nanoclusters at the atomic dispersion along with Fe and Co atoms as seen individually in the electron map (Figure 3g, Fe and Co atoms). The EDS mapping from a particle shows the presence of Co and Fe in the same region, indicating atomic nanoclusters, excluding the presence of alloy particles as supported by the XRD pattern. While comparing with controlled sample Fe-SA950NC which exhibit slightly concave rhombododecahedron shape with a hierarchical rough surface, revealing the conformal structure due to pyrolysis [27]. The AC-HAADF-STEM electron image of Fe-SA950NC is shown in Figure S5 showing the Fe atoms in elemental mapping. X-ray photoelectron spectroscopy (XPS) was used to investigate the chemical states (element composition) of the $Fe_A$-$Co_A$/MWCNT-NC at the surface by $Ar^+$ etching. The elemental contents of C, N, Fe, Co, O were analyzed by the deconvolution of corresponding peaks for effective fitting analysis with Fe-atomic content attributed to the specific surface areas and exposed active sites. Distinct Fe and Co atom signals were detected due to the content being above the detection limit, wherein a Fe $2p_{3/2}$ and $2p_{1/2}$ peaks at 710 and 715 eV were observed, respectively, suggesting the +3 valence of Fe–$N_x$ sites. Three significant peaks in the deconvoluted Co $2p_{3/2}$ and $2p_{1/2}$ at 781 and 786 eV suggest the presence of $Co^{+3}$ atom sites (Figure 4a,b). N 1s spectra (Figure 4c) correspond to significant pyridinic-N (399.5 eV), pyrrolic/graphitic-N/C–N (402 eV) without any oxidized-N (404 eV), providing evidence of the co-existence of varied types of Ns with significant pyridinic N in the MWCNT-NC matrix wherein the pyridinic-N can play a substantial role in forming the isolated FeCo–$N_x$ structure [43]. Thus, a significant ∼20% pyridinic-N can help form a higher percentage of single Fe-atom sites along with a significantly high graphitic-N/pyrrolic-N ∼58% at 401 eV broad peak, indicating the formation of an increased number of Fe-N and Co-N active sites in $Fe_A$-$Co_A$/MWCNT-NC. Additionally, the high-resolution Fe 2p spectra of $Fe_A$-$Co_A$/MWCNT-NC were well-fitted with $Fe^{+2}$ species without the presence of any metallic $Fe^0$ at 707.3 eV [44]. $Fe^{+2}$ is a major component in Fe $2p_{3/2}$ and $2p_{1/2}$ (Figure 4a) at 710.9 and 715.6 eV, respectively. For a high-resolution Co $2p_{3/2}$ and Co $2p_{1/2}$ spectral peaks at 781.7 and 786.4 eV (satellite peak) respectively which correspond to $Co^{+2}$ [44]. The high-resolution C 1s spectra (Figure 4d) show the typical C–N peak at 285.5 eV, confirming the successful N-doping in MWCNT-NC. The deconvoluted. C 1s XPS spectra show three different significant deconvoluted peaks at 284.6 and 285.4 eV, corresponding to C=C and C–N functionality on the MWCNT-NC matrix holding Fe and Co-SA. O 1s XPS spectra (Figure 4e) demonstrate the O–C=O and C-OH peaks in the deconvoluted spectra.

## 2.2 | Oxygen Reduction Reaction (ORR) in RRDE

The ORR performance of the as-prepared $Fe_A$-$Co_A$/MWCNT-NC was investigated by rotating ring disk electrode (RRDE) in 0.1 M KOH in a three-electrode system by applying an $O_2$-saturated condition. In this process, the ORR was benchmarked Pt/C, and a FeSA950NC electrode served as the control sample. All recorded potentials were referenced with respect to the reversible hydrogen electrode (RHE). As illustrated in Figure 5a, $Fe_A$-$Co_A$/MWCNT-NC exhibits superior ORR activity with respect to reference Pt/C by showing a higher onset potential

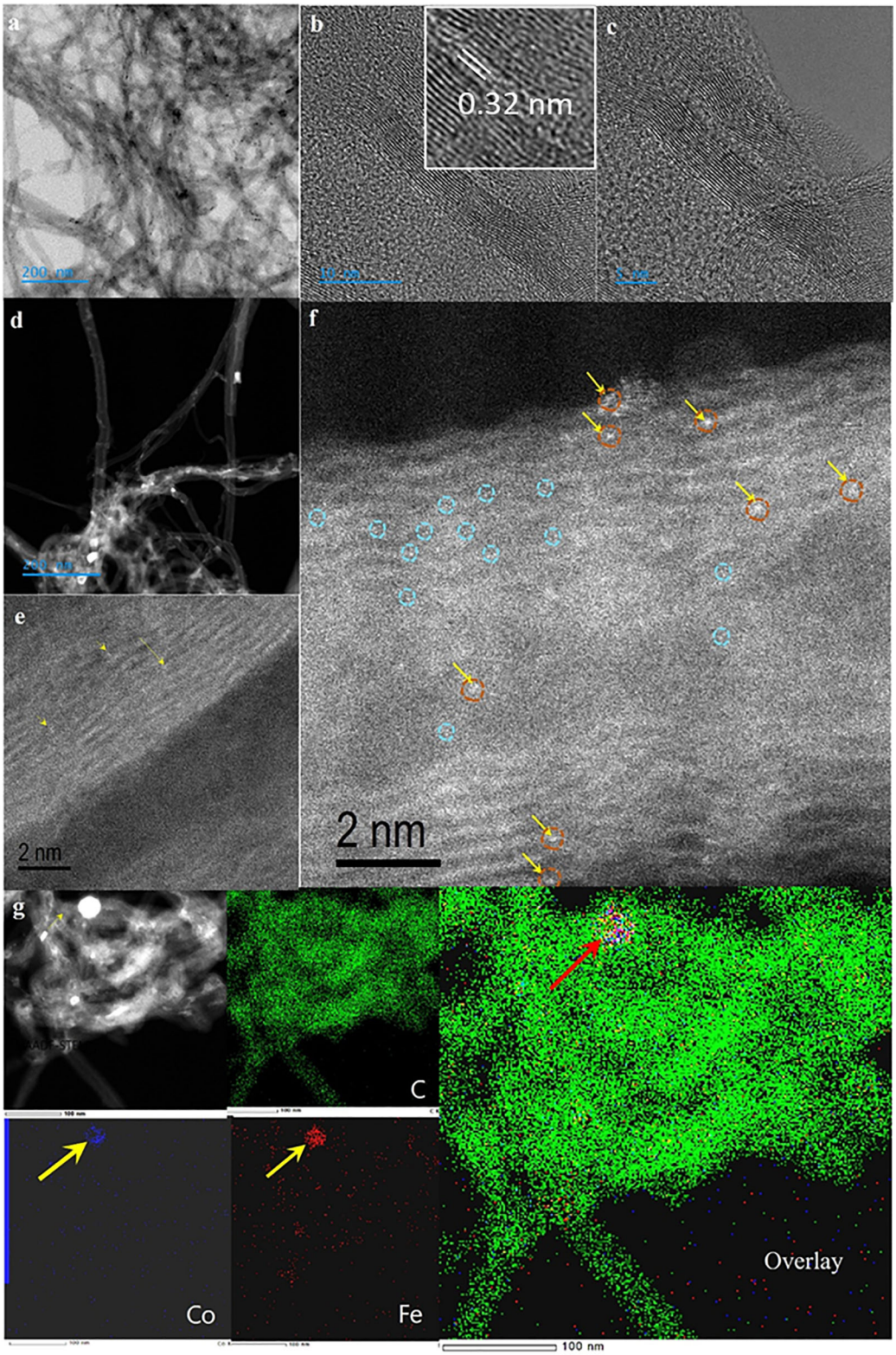


**FIGURE 3** | (a) TEM image. (b,c) HR-TEM images. (d) Low magnification STEM image. (e,f) HAADF-STEM images showing the presence of dual-atoms. (g) HAADF-STEM EDS mapping of elements C, Co, Fe, and overlay.

(Eonset) of 0.875 V and a half-wave potential ($E_{1/2}$) of 0.783 V, outperforming Pt/C (0.812 V $E_{onset}$ and 0.733 V $E_{1/2}$) and FeSA950NC (0.000 V $E_{onset}$ and 0.000 V $E_{1/2}$). This shows the outperforming features of $Fe_A$-$Co_A$/MWCNT-NC as compared to similar single-atom materials as an electrode. As shown in the RRDE linear sweep voltammetry (LSV) polarization curve at a scan rate of 5 mV $s^{-1}$ at 1600 rpm (Figure 6a) with a progressively enhanced Fe-SA to $Fe_A$-$Co_A$/MWCNT-NC concerning the reference Pt/C with improved half-wave potential ($E_{1/2}$) to 0.83 V versus reversible hydrogen electrode (RHE), indicating that

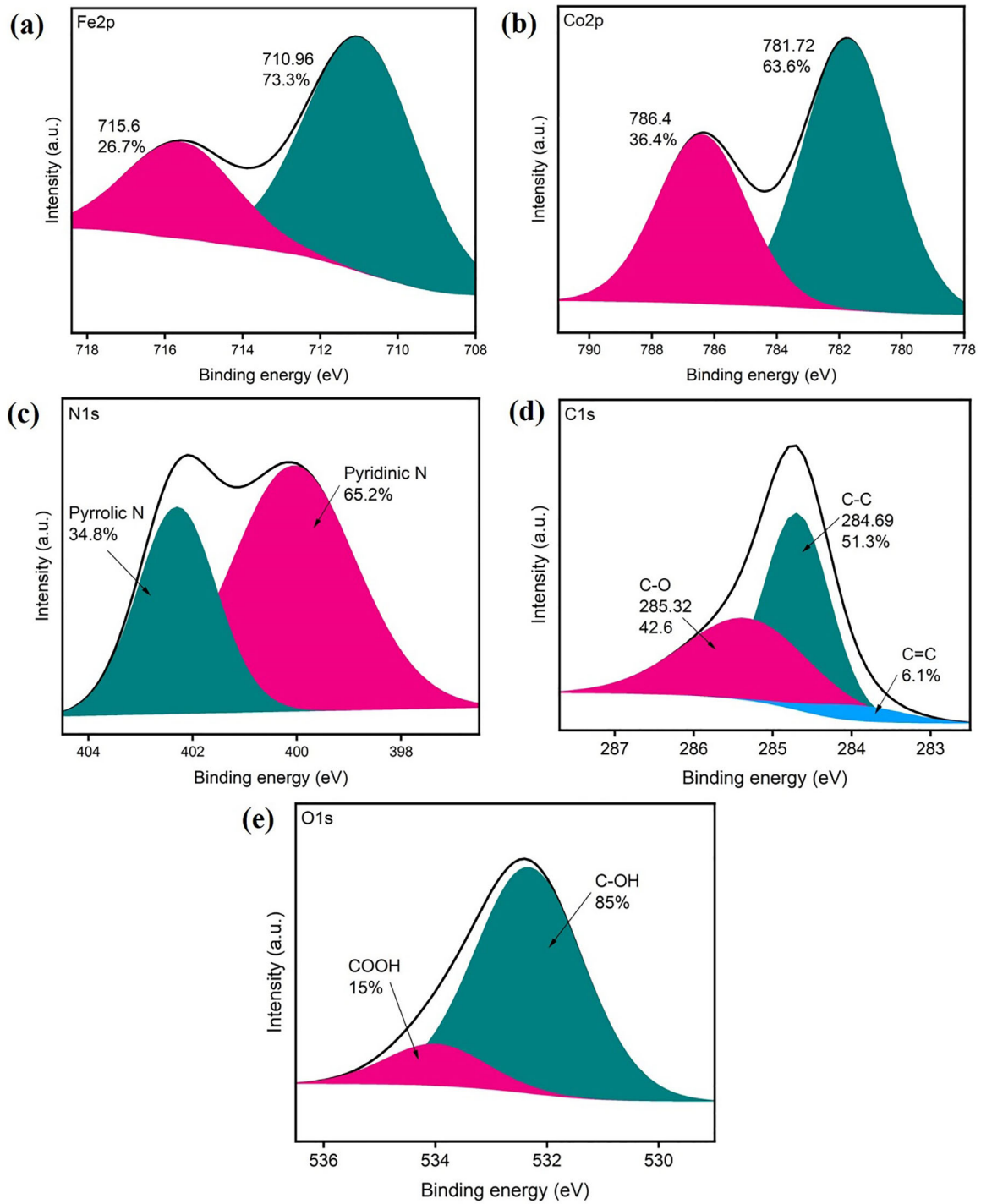


**FIGURE 4** | (a) Fe $2p_{1/2}$ and Fe$2p_{3/2}$ XPS spectra with percentage of contribution. (b) Co $2p_{1/2}$ and Co $2p_{3/2}$ XPS spectra. (c) N 1s XPS. (d) C 1s XPS. (e) O 1s XPS of $Fe_A$-$Co_A$/MWCNT-NC.

the ORR activity could be boosted by increasing the loading of $Fe_A$-$Co_A$/MWCNT-NC active site, which is in good accord with reported ORR electrodes [45, 46]. $Fe_A$-$Co_A$/MWCNT-NC provided a highly impressive onset potential ($E_{onset}$) of 0.875 V and a half-wave potential ($E_{1/2}$) of 0.783 V, outperforming Pt/C (0.812 and 0.733 V). These results confirm that the presence a di-atomic environment of a $Fe_A$-$Co_A$-$N_6$ is more effective for tuning the electronic structure of Fe−Co−N−C sites, leading to enhanced ORR activity. Corresponding Tafel plots for ORR on $Fe_A$-$Co_A$/MWCNT-NC were obtained based on the LSV curve to evaluate the kinetics of ORR. Figure 5b represents kinetic current density ($J_k$) of 18 mA $cm^{-2}$ at 0.8 V, superior to Pt/C (1 mA $cm^{-2}$) and FeSA950NC (2 mA $cm^{-2}$). As presented in Figure 5c, the $Fe_A$-$Co_A$/MWCNT-NC offers the smallest Tafel slope 53.3 mV $dec^{-1}$ as compared to Pt/C (290 mV $dec^{-1}$), signifying it owns the fastest ORR kinetics and an excellent ORR activity as compared with FeSA950NC (Tafel slope 119 mV $dec^{-1}$). This substantiates its faster kinetics and lower of energy barrier. The kinetic current density ($J_k$) of $Fe_A$-$Co_A$/MWCNT-NC was measured at 0.85 V, which was found to be higher than that

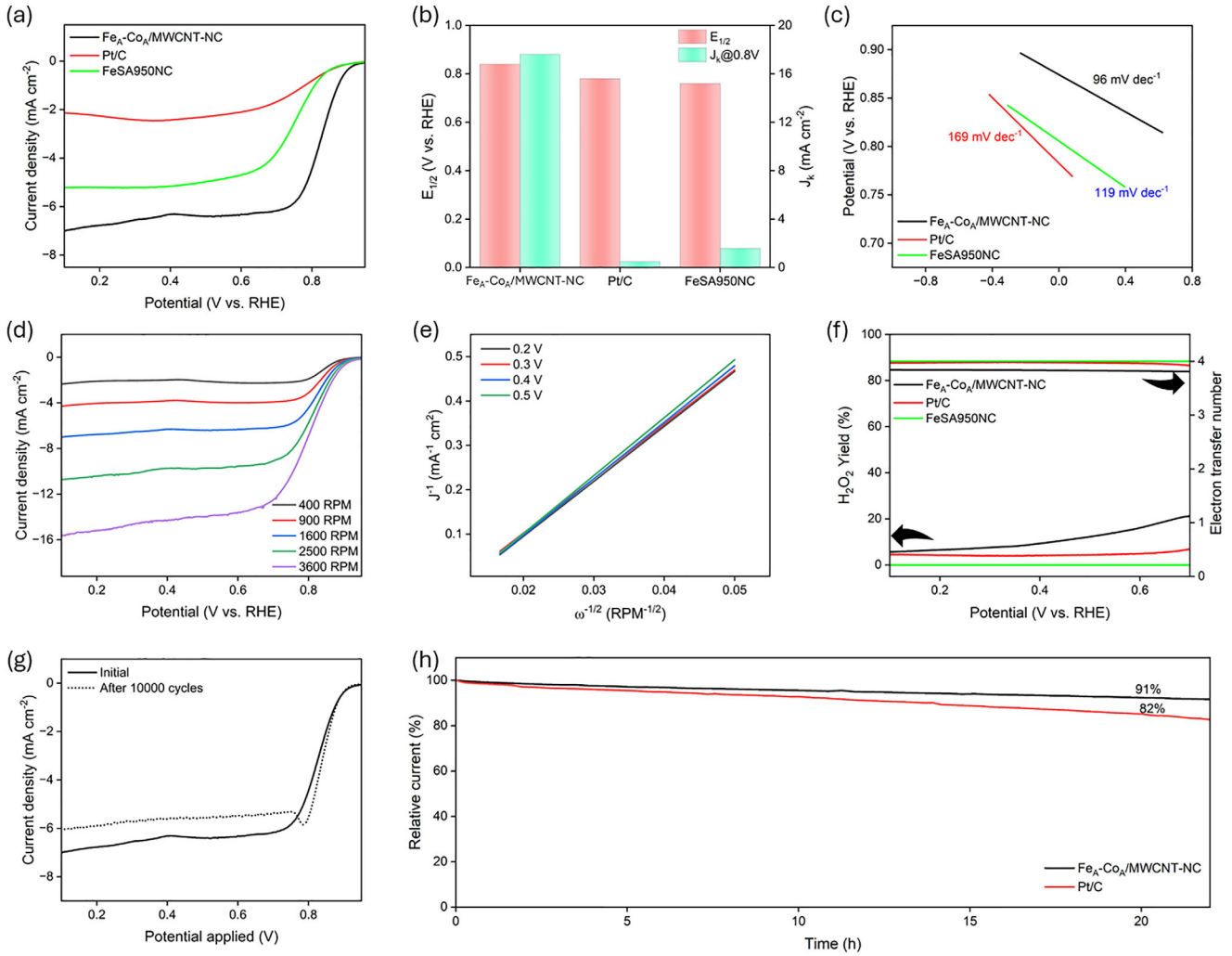


**FIGURE 5** | ORR electrocatalytic performance of $Fe_A$-$Co_A$/MWCNT-NC, Pt/C, and FeSA950NC in $O_2$-saturated 0.1 m KOH solution. (a) RRDE polarization curves at a scan rate of 5 mV $s^{-1}$ at 1600 rpm; (b) $J_k$ at 0.8 V, and $E_{1/2}$ for the set; (c) The ORR Tafel plots. (d) Polarization curve at the rotating speed from 400 to 3600 RPM of $Fe_A$-$Co_A$/MWCNT-NC; (e) The responding K–L plots for $Fe_A$-$Co_A$/MWCNT-NC; (f) Electron transfer number (top) and hydrogen peroxide yield (bottom) obtained from RRDE; (g) ORR polarization curve before and after 10000 CV cycles in $O_2$-saturated 0.1 m KOH at 1600 RPM for $Fe_A$-$Co_A$/MWCNT-NC. (h) Chronoperometric curves of $Fe_A$-$Co_A$/MWCNT-NC and Pt/C at 0.75 V.

of FeSA950NC and Pt/C, demonstrating the effectiveness of Co inclusion via a chemical technique for enhancing ORR activity and reaction kinetics. To gain a deeper insight into the ORR, the RRDE tests and the Koutecky–Levich (K–L) method were employed to investigate the ORR on FeA-CoA/MWCNT-NC at various rotational speeds ranging from 400 to 3600 rpm (Figure 5d). The resulting K-L plots were linear and parallel, suggesting a first-order ORR (Figure 5e) [47]. Rotating ring-disk electrode data were recorded to assess the ORR selectivity of $Fe_A$-$Co_A$/MWCNT-NC. According to the K-L equation, the number of transferred electrons ($n$) on the $Fe_A$-$Co_A$/MWCNT-NC during ORR was calculated to be 3.815 with a very low hydrogen peroxide ($H_2O_2$) yield of less than 5% over a wide range of ORR potentials (Figure 5f), with dominance of four-electron ORR pathways and excellent selectivity for electroreduction of $O_2$ to $OH^-$. As illustrated in Figure 5f, $Fe_A$-$Co_A$/MWCNT-NC demonstrates a very low $H_2O_2$ formation rate in the potential region of 0.2 to 0.4 V, and a high electron transfer number (n) ranging between 3.80 to 3.82. When the percentage of $H_2O_2$ formation is higher by an atomic site containing electrode (~3.5%) as compared to Pt/C standard (~2.8%), a lower electron transfer number (n) 3.93 to 3.96 at 0.2 to 0.6 V potential range was noted [37]. This electron transfer number (n) enhanced to ~3.97 at a higher potential 0.8 V as compared to Pt/C. This highlights a 4-electron ORR pathway of $Fe_A$-$Co_A$/MWCNT-NC in alkaline media [35]. This result is consistent with the K-L plots obtained from the LSV data collected at varying rotation speeds (Figure 5d). The Pt/C reference electrode offers an average electron transfer of 3.92, demonstrating a $4e^-$ mechanism ORR polarization curve before and after 10000 CV at 5 mV $s^{-1}$ cycles in $O_2$-saturated 0.1 m KOH at 1600 RPM (Figure 5g). Furthermore, $Fe_A$-$Co_A$/MWCNT-NC exhibits superior tolerance to methanol poisoning and excellent stability without significant changes in the electronic environment for the active Fe sites. Normalized i-t curves (Chronoperometric curves) of $Fe_A$-$Co_A$/MWCNT-NC and Pt/C at 0.75 V (Figure 5h) reveal that stability retention of maximum 91% until 22 h as compared to slightly less stability 82% for Pt/C, suggesting $Fe_A$-$Co_A$/MWCNT-NC consists of no significant current attenuation due to a higher conductive nature as a result

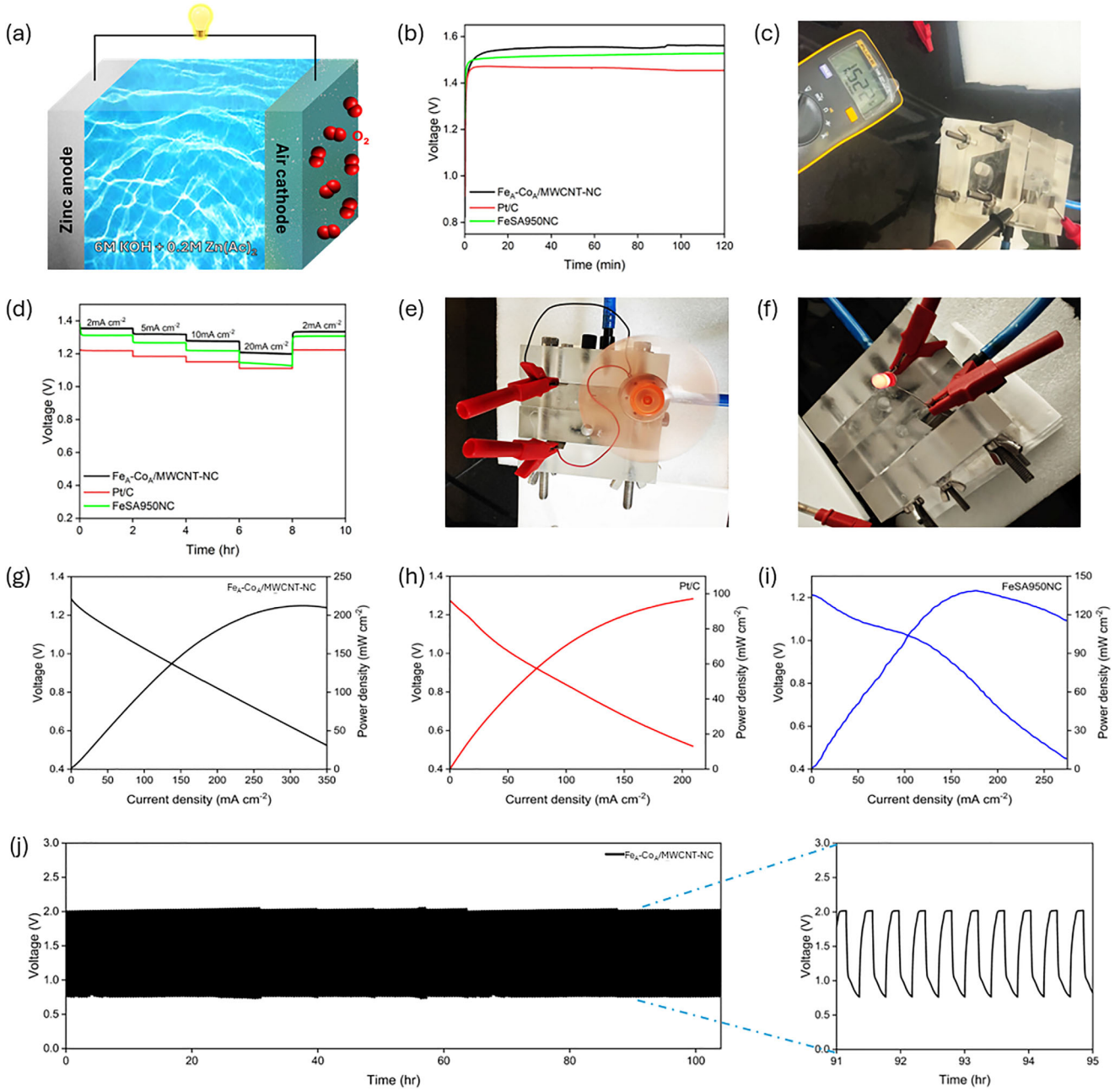


**FIGURE 6** | Performance evaluation of ZABs equipped with $Fe_A$-$Co_A$/MWCNT-NC as the air cathode at 25°C. (a) Design of a ZAB with air cathode $Fe_A$-$Co_A$/MWCNT-NC. (b) Open circuit voltages of the ZAB based on $Fe_A$-$Co_A$/MWCNT-NC and Zn-anode and the corresponding power density curve of $Fe_A$-$Co_A$/MWCNT-NC as compared to that of Pt/C as cathode. (c) OCV measured with a multimeter. (d) Galvanostatic discharge curves with discharging plateaus with current densities from 2 to 20 mA $cm^{-2}$ of $Fe_A$-$Co_A$/MWCNT-NC, Pt/C, and FeSA950NC cathodes. (e) An extension of ZAB to connected to an electrical charge-driven fan, (f) An extension of ZAB to a LED bulb. Discharging polarization curves and the corresponding power density plot of (g) $Fe_A$-$Co_A$/MWCNT-NC as a cathode. (h) Pt/C as cathode. (i) FeSA950NC. (j) Charge–discharge cycling performance of ZAB with cycling stability at 5 mA $cm^{-2}$ for $Fe_A$-$Co_A$/MWCNT-NC.

of dual-atoms (Fe−Co) synergism in the MWCNT-driven carbon structure.

ORR polarization curve before and after 10000 CV cycles in $O_2$-saturated 0.1m KOH at 1600 RPM is shown in Figure 5g. A synergistic effect of $Fe_A$-$Co_A$ unit with excellent all-around ORR performance is considered, as compared to the Pt/C electrocatalyst. $Fe_{SA}$ and $Co_{SA,}$ both units, are determined to be critical to the all-around ORR performance of $Fe_A$-$Co_A$/MWCNT-NC. When comparing the LSV curves of Pt/C and $Fe_A$-$Co_A$/MWCNT-NC (Figure S4a), the latter exhibits more positive onset potential (0.98 V) and half-wave potential (0.85 V) toward ORR as compared to Pt/C. The superior ORR kinetics of $Fe_A$-$Co_A$/MWCNT-NC is evident as it demonstrates the smallest Tafel slope (0.47 mV $dec^{-1}$) and highest kinetic current density (8.33 mA $cm^{-2@0.85\,V}$) (Figure S4b). Moreover, $Fe_A$-$Co_A$/MWCNT-NC exhibits an electrochemical double layer capacitance ($C_{dl}$) of mF $cm^{-2}$ and mass activity of 97.6 A $g^{-1,}$ than the control Pt/C. Figure S4c

and Polarization curve (Figure S4d) at the rotating speed from 400 to 3600 RPM; d) The responding K–L plots derived from LSV curves indicate ORR kinetics are close to the $O_2$-diffusion process. The electron transfer number was determined as (n) 3.66, which suggests a direct 4e reduction pathway during the ORR process. Electron transfer number (top) and hydrogen peroxide yield (bottom) obtained from RRDE (Figure 5f) support that both electron transfer numbers in $Fe_A$-$Co_A$/MWCNT-NC. Figure 5g shows the ORR polarization curve before and after 10000 CV cycles in $O_2$-saturated 0.1 m KOH at 1600 RPM.

## 2.3 | $Fe_A$-$Co_A$/MWCNT-NC as ZAB Cathode

Rechargeable ZABs require an air-cathode with electrocatalysts to offer oxygen reduction reaction (ORR) activity and stability [48]. The engineering of an electrode would enable an air cathode to achieve higher efficiency for ZABs with higher energy density than an air cathode without the desired surface design [49]. The effectiveness of $Fe_A$-$Co_A$/MWCNT-NC as an electrode is evaluated by incorporating it as the cathode of a ZAB as a designed glass cell with a working electrode and Zn metal plate as an anode counter electrode, as shown in image of the assembled ZAB cell (Figure 6a). $Fe_A$-$Co_A$/MWCNT-NC and Pt/C as electrocatalyst loaded in the carbon paper as the air cathode and a 6.0 M KOH/0.2 M $Zn(Acetate)_2$ mixed solution as the electrolyte. As a comparison, Pt/C was assembled to the air cathode to make a direct comparison with $Fe_A$-$Co_A$/MWCNT-NC, along with FeSA950NC to reveal the effect of dual-atom sites. As shown in Figure 6b, the $Fe_A$-$Co_A$/MWCNT-NC-based ZAB exhibited an open-circuit voltage 1.522 V, superior to 1.47 V reached in the Pt/C-based ZAB, as real-time voltage measured with a multimeter (Figure 6c).

Figure 6d displays the galvanostatic discharge curves of Zn– air battery with $Fe_A$-$Co_A$/MWCNT-NC, Pt/C, and FeSA950NC the discharge plateau decreased slowly with the current density from 2 to 20 mA $cm^{-2}$. As illustrated in Figure 6e,f, a fan and light-emitting diode (LED) can be powered by ZABs assembled with $Fe_A$-$Co_A$/MWCNT-NC, implying its promise as an electrocatalyst in practical applications. The discharge polarization and power density curves were displayed in Figure 6g–i, the maximum power density of $Fe_A$-$Co_A$/MWCNT-NC-based Zn–air battery, outperforms that of Pt/C and FeSA950NC based Zn-air batteries. Peak Power density for $Fe_A$-$Co_A$/MWCNT-NC is 213 mW $cm^{-2}$ and for Pt/C and FeSA950NC are 97 mW $cm^{-2}$ and 138.8 mW $cm^{-2}$ respectively. At the discharge current density of 10 mA $cm^{-2}$, the battery with $Fe_A$-$Co_A$/MWCNT-NC presents voltage plateaus of ≈1.27 V, which is higher than that of Pt/C catalyst (1.15 V). Moreover, the discharge resumes reversibly when the current density reduces to 2 mA $cm^{-2}$, suggesting remarkable discharge rate performance and good reversibility of $Fe_A$-$Co_A$/MWCNT-NC based Zn–air battery. The cycling stability was estimated by continuous galvanostatic discharge and charge at 5 mA $cm^{-2}$ for 104 hrs (Figure 6j).

To probe the structural stability of the dual-atomic sites, XPS analysis was performed on the $Fe_A$-$Co_A$/MWCNT-NC cathode after long-term ZAB cycling. As shown in Figure S7, the Fe 2p and Co 2p spectra exhibit only minor positive shifts (~0.2–0.3 eV) in binding energies, indicating slight surface oxidation without significant demetallation or formation of metallic species (Figure S7a,b). The retention of pyridinic-N and M–N contributions in the N 1s spectrum confirms the robustness of the Fe–$CoN_6$ coordination environment. These results, combined with the excellent activity retention (91% after 22 h chronoamperometry and stable voltage plateaus over 100+ h), demonstrate the superior durability imparted by the synergistic charge redistribution in the bridging dual-atom configuration supported on the MWCNT-NC nanofiber matrix.

## 2.4 | Density Functional Theory (DFT) Simulation on Single-Atom Arrangement

The ORR process on the graphene-based dual-atom catalyst is schematically shown in Figure 7a, emphasizing the stepwise adsorption and change of intermediates. With DFT optimization, the $FeN_4$ and $CoN_4$ sites integrated into the graphene lattice maintained their structural integrity and displayed a well-preserved $M-N_4$ (M: Fe and Co) coordination environment, shown in Figure 7b,c. To ensure the reliability of the optimized geometries, an energy validation analysis was performed by comparing DFT energies of MLIP (MACE-MP-0) pre-optimized structures with fully DFT-relaxed configurations. The resulting energy correlation plot (Figure S8) demonstrates strong agreement, confirming that the MLIP-relaxed geometries are consistent with DFT minima and are suitable as initial structures for accurate DFT calculations. Stable coordination is further established by the individual metal-nitrogen bond lengths. The Fe—N bonds in $FeN_4$ are 1.87Å [50], while the Co—N bonds in $CoN_4$ are 1.85 Å, which is also in good agreement with the reported value [51]. These bond distances demonstrate strong metal-nitrogen coordination and validate the strong active sites.

After confirming the structure stability of the single-atom model, we analyzed the ORR activity on the single-atom consisting electrode. Twenty potential adsorption sites around the $FeN_4$ and $CoN_4$ centers were systematically tested before the final adsorption positions for the reaction pathway were chosen. All ORR intermediate calculations were conducted using the configuration with the lowest adsorption energy, which was determined to be the most energetically favorable site. For the analysis of the ORR activity, all the important oxygen intermediates—$O_2$*, OOH*, O*, OH* were successively absorbed on $FeN_4$ and $CoN_4$ sites. Figures S9 and S10 display the optimized structure of all the configurations of these intermediates obtained from MLIP-driven DFT approach. As shown in Figure S8, when $O_2$* binds to $FeN_4$ center in a tilted configuration, generating two Fe—O bonds (1.96 Å) while the O—O bond (1.33 Å) remains nearly parallel to the graphene plane, indicating strong chemisorption. With further protonation, OOH* stays end-on after proton-electron addition with Fe-O (1.85 Å), O-O (1.47 Å) and O-H (0.97 Å). Strong chemisorption is characterized by a shorter Fe—O bond of 1.62 Å, which is formed when the O* intermediate adsorbs more strongly in a vertical end-on mode following O—O bond cleavage. Lastly, OH* maintains its coordination in an end-on geometry with a Fe—O distance of 1.85 Å and O-H is 1.1 Å, indicating a moderate binding ability that makes OH removal easier. Similar to $CoN_4$ Figure S8, ORR depicting shorter Co—N bond (1.85 Å), the $CoN_4$ site has comparable adsorption behavior but somewhat weaker binding strengths. By interacting with Co in a tilted end-on

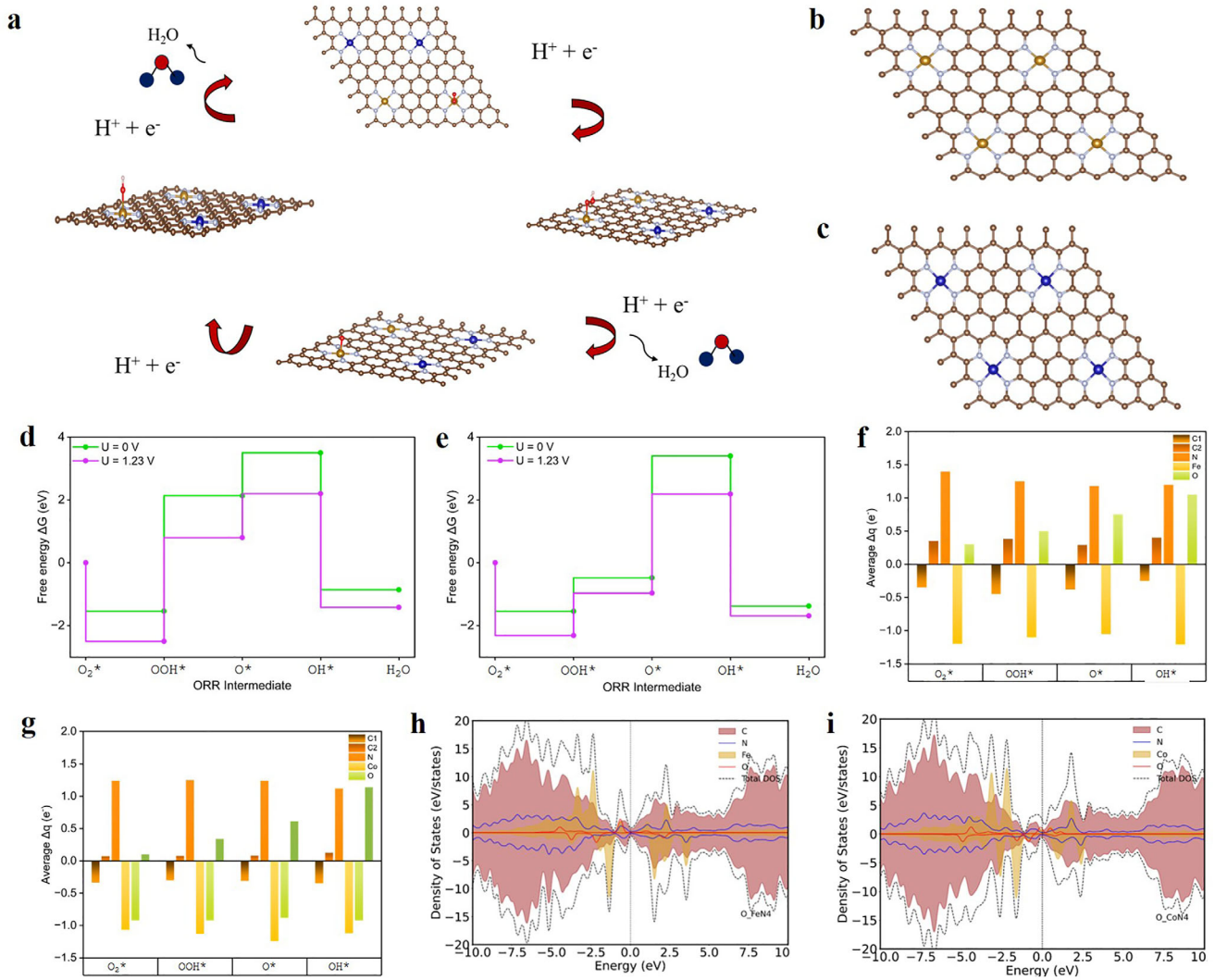


**FIGURE 7** | (a) Schematic representation of the ORR pathway with a dual-atom environment on a graphene lattice. DFT-optimized single-atom system structures: (b) $FeN_4$ and (c) $CoN_4$, where brown, yellow, blue, and grey spheres represent C, Fe, Co, and N atomic species respectively. ORR free-energy profiles showing the potential-determining steps for (d) $FeN_4$ and (e) $CoN_4$. Charge redistribution during ORR intermediates with average Bader charge variation per atom for (f) $FeN_4$ and (g) $CoN_4$. Partial density of states (PDOS) for the potential-determining step for (h) $FeN_4$ and (i) $CoN_4$, showing the importance of electronic structure to ORR activity.

configuration, the $O_2$* intermediate maintains an O–O distance of 1.24 Å and forms a Co—O bond of approximately 2.39 Å. The O—O bond is activated when the Co—O and O—O bonds shorten to approximately 1.80 and 1.46 Å, respectively, upon protonation to OOH*. The OH* intermediate stabilizes with a moderate Co-O distance of approximately 1.86 Å, whereas the O* species binds through a single strong Co—O bond of approximately 1.64 Å. These patterns demonstrate that, in comparison to $FeN_4$, $CoN_4$ also offers a stable but marginally weaker active center, which may have an impact on the overall ORR energetics. Following the determination of the $FeN_4$ and $CoN_4$ sites' structural stability and adsorption behavior, the free-energy change (ΔG) for each step in the ORR pathway was calculated within the DFT framework, as shown in Figure 7d,e.

Figure 7d represents the ORR profile for $FeN_4$. Strong oxygen species adsorption is demonstrated by the $FeN_4$ site, which is compatible with the previously reported shorter Fe—O bond lengths. The OH* formation step exhibits the largest uphill barrier (~3.50 eV) at U = 0 V, suggesting that the potential-determining step (PDS) is the conversion of O*-OH* [52]. This significant endergonic step shows that, despite $FeN_4$ strong oxygen binding, the final proton-electron transfer required for OH* production demands an even higher overpotential. In contrast, $CoN_4$ catalyst demonstrates a comparable ORR trend which is shown in Figure 7e, but with generally reduced adsorption strengths and slightly lower intermediate stabilization. With a similar uphill free-energy barrier of approximately 3.40 eV, the conversion of O—OH** is also the most challenging step for $CoN_4$. This indicates that, despite having the same PDS, $CoN_4$ is slightly more advantageous in terms of overpotential than $FeN_4$ because of its weaker oxygen binding, which lowers the energy needed for intermediate transformations.

The electronic behavior of the $FeN_4$ and $CoN_4$ centers during intermediate adsorption is further clarified by the Bader-charge

analysis after the ORR energetics. Figure 7f illustrates the Bader charge analysis for $FeN_4$. In $FeN_4$, $O_2$ adsorption results in Fe losing electron density and the O atoms gaining charge, which is consistent with strong electron back-donation and O-O activation. Additionally, just a fraction of charge is acquired by the nearby N atoms, indicating their role in maintaining the Fe—O bond. When OOH* is formed, Fe continues to undergo charge reduction, but O atoms gain charge and H shows a small charge loss, demonstrating proton-electron coupling. Compared to $FeN_4$, Bader charge analysis in $CoN_4$ shown in Figure 7g depicts an alternate electronic action during ORR intermediate adsorption. Co experiences moderate electron loss upon $O_2$ adsorption, while the O atoms acquire charge, suggesting a reduced significant back-donation impact than in $FeN_4$. The neighboring N atoms exhibit little charge shift, indicating a less significant contribution to the stability of the Co-O interaction. Co keeps on losing electron density as the reaction moves toward OOH* formation, but to a smaller extent than Fe, indicating a more restricted electron interaction. In OOH*, the H atom displays an insignificant charge loss and the O atoms gain charge, which is in line with electron-proton pairing. We carried out a projected density of states (PDOS) study for arrangement at the PDS, namely OH* adsorption, to better understand the electronic behavior of $FeN_4$ during the ORR process.

For the $FeN_4$ site during the OH* adsorption step Figure 7h, the PDOS reveals a considerable rise in O-*2p* states around the Fermi level, along with noticeable widening and shifting of the Fe-*3d* states. This considerable Fe-O orbital overlap implies substantial hybridization and validates the Bader analysis, which validates that charge transfer from Fe to the OH* adsorbate occur. On the other hand, the PDOS reveals a small rise in O-*2p* contribution close to the Fermi level at the $CoN_4$ site Figure 7i after OH* adsorption, but the Co-*3d* states shift more gradually with minimal broadening. A substantially weaker hybridization is implied by this finding, showing a lowered Co-O interaction strength that correlates to the weaker OH* binding capacity that has been found for $CoN_4$.

## 2.5 | Density Functional Theory (DFT) Simulation on Dual-Atom Arrangement

We investigated the dual-atom configuration, in which Fe and Co are integrated within adjacent $N_4$ moieties in a shared graphene lattice, after determining the electrochemical activity trends of the $FeN_4$ and $CoN_4$ single-atom sites. Several dual-atom geometries have been examined to determine the most stable and electrochemically beneficial configuration. One bridging configuration, in which Fe and Co share oxygen-binding functions through a bridging interaction and five lateral Fe−Co configurations where both metals are positioned side by side within adjacent $N_4$ pockets, were methodically investigated. After assessing the stability of the structure, the energetically most favorable configuration was determined. There was only one feasible configuration for the bridge-style dual-atom arrangement, which was additionally optimized and incorporated for comparison. The DFT-optimized structures of the Fe−Co−N lateral arrangement and the Fe−Co−N bridging configuration are shown in Figure 8a,b. The two metal atoms (Fe and Co) in the bridging-type Fe-Co dual-atom configuration coordinate along the zigzag direction of the carbon frameworks because they occupy adjacent $N_4$ coordination spaces that share a common surface within the graphene lattice. This arrangement ensures effective electronic transfer interaction between the two active centers by creating a structurally integrated bridge between Fe and Co, which produces a well-defined Fe−N and Co−N coordination (both 1.87 Å) and a Fe−Co separation of roughly 2.46 Å.

The most stable lateral Fe−Co dual-atom configuration was identified as well and examined after the bridging-type arrangement. Instead of sharing an edge, the Fe and Co atoms are arranged side by side within two adjacent $N_4$ coordination regions in this optimized lateral geometry. With Fe—N and Co—N bond lengths of about 1.88 Å and 1.85 Å, respectively, each metal center maintains its intrinsic square-planar M-$N_4$ coordination, suggesting strong structural stabilization comparable to the SAC counterparts. The lateral arrangement preserves a distinct spatial separation between the two metal sites while facilitating beneficial catalytic behavior through the $\pi$-conjugated graphene network, in contrast to the bridging model where Fe and Co share an interconnected electronic pathway.

A similar approach was used for the Fe−Co dual-atom after the structural stability and ORR behavior of the $FeN_4$ and $CoN_4$ single-atoms were established. The most stable bridging-type and lateral-type configurations were chosen for extensive ORR electrolysis after several Fe−Co arrangements were tested. All-important ORR intermediates, including $O_2$*, OOH*, O*, OH*, were similarly sequentially adsorbed on the Fe−Co dual-atom active center. Figures S11 and S12 show the optimized adsorption geometries for each intermediate on the Fe−Co atom site. To determine the preferred reaction pathway and adsorption geometries for the lateral Fe−Co dual-atom arrangement, all ORR intermediates—$O_2$*, OOH*, O*, OH* were individually adsorbed. Fe and Co occupy adjacent but separate $N_4$ sites in this configuration, enabling both metals to participate in oxygen binding. Due to its relatively greater oxygen affinity, the oxygen reduction intermediates exhibit a clear preference for the Fe center [53]. Here, computationally, observed the 'synergistic imbalance' feature having Fe as a prominent ORR active site. To further quantify this preferential adsorption behavior, the adsorption energies of key ORR intermediates (O*, $O_2$*, OH*, and OOH*) on Fe-$N_4$ and Co-$N_4$ active sites were systematically evaluated (Figure S13). The results consistently show stronger adsorption at Fe sites, particularly for OH* and OOH* intermediates, confirming the dominant role of Fe in stabilizing reaction intermediates and facilitating ORR kinetics. $O_2$* preferentially binds at the Fe site instead of the Co site during the first adsorption step, forming a Fe—O bond of about 1.98 Å while the O—O bond is only slightly perturbed at about 1.11 Å, suggesting a tilted adsorption configuration that is largely regulated by Fe. The OOH* intermediate remains attached at Fe in an end-on configuration upon proton-electron addition, demonstrating Fe−O and O−O distances of approximately 1.99 and 1.23 Å, respectively. After O—O bond cleavage, Co is still electronically coupled but not directly involved in adsorption, while the O* species binds to Fe more strongly through a shortened Fe−O distance of about 1.79 Å. Last, OH* stays coordinated at the Fe site with an O−H distance of about 1.00 Å and a Fe—O bond length

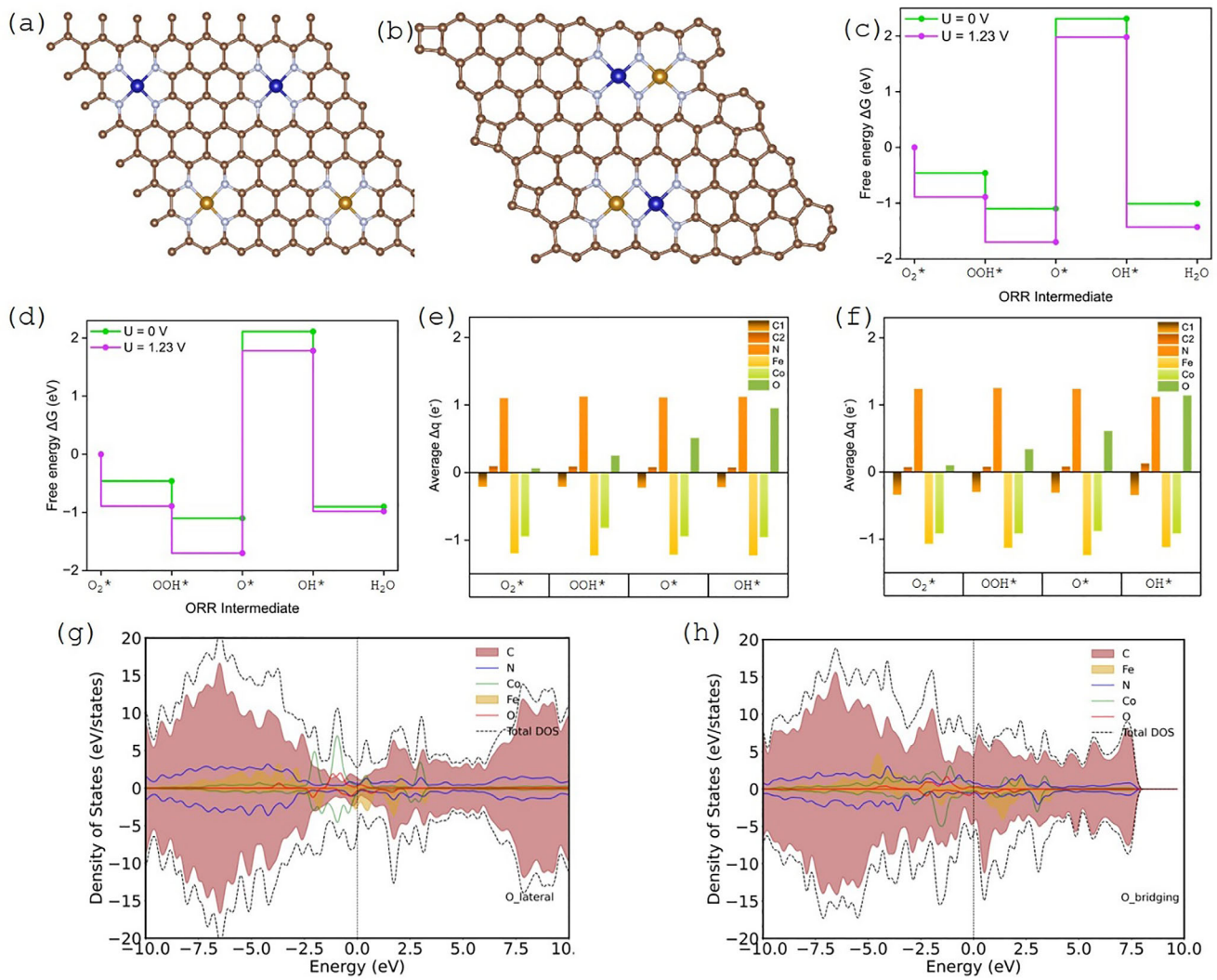


**FIGURE 8** | (a) DFT-optimized dual-atom structures: Fe−Co−N lateral and (b) Fe−N−Co Bridging, where brown, yellow, blue, and grey spheres represent C, Fe, Co, and N atomic species, respectively. ORR free-energy profiles showing the potential-determining steps for (c) Fe−Co−N lateral and (d) Fe−N−Co Bridging. Charge redistribution during ORR intermediates is shown in (e) the average Bader charge variation per atom for Fe−Co−N lateral and (f) Fe−N−Co Bridging. (g) Partial density of states (PDOS) for the PDS for Fe−Co−N lateral and (h) Fe−N−Co Bridging, showing the importance of electronic structure to ORR activity.

of about 1.98 Å, indicating moderated binding that promotes OH desorption.

In contrast, the bridging-type Fe−Co dual-atom has a more compact system than the lateral configuration, with Fe and Co located in nearby $N_4$ coordination spaces that have a common boundary inside the graphene framework. $O_2$* preferentially binds at the Fe site during the ORR process, resulting in an end-on configuration with an O−O distance of ~1.24 Å and a Fe—O bond length of ~1.97 Å, indicating higher activation than the lateral configuration. Following proton-electron addition, Co stays electronically active within the shared coordination surroundings but does not establish a direct bond with the intermediate, while OOH* persists to adsorb at Fe with Fe−O and O−O distances of approximately 1.96 and 1.33 Å, respectively. Fe's dominant oxygen affinity is further proven by the O* species stabilizing at the Fe site through a shortened Fe—O bond of about 1.82 Å upon O−O dissociation. With a Fe-O distance of about 1.90 Å and an O—H bond length of about 1.00 Å, the final OH* intermediate also preferably aligns at Fe, exhibiting a moderate binding strength favorable to OH desorption.

To investigate how dual-metal arrangements impact reaction dynamics, the ORR free-energy profiles of the Fe−Co dual-atoms were examined. Figure 8 represents the ORR profile for the lateral arrangement. The OH* formation step is identified as the PDS by the ORR free-energy profile of the lateral Fe−Co dual-atoms, with an uphill barrier of approximately 2.31 eV at U = 0 V. The PDS is still the OH* formation step in the bridging dual-atom shown in Figure 8d, but the barrier drops to about 2.11 eV, indicating increased synergistic effects between Fe and Co that lower the overpotential and enable intermediate transformation [54]. The improvement is mainly caused by the bridge geometry's lower Fe−Co distance and improved metal-metal connection, which improves orbital overlap while enabling electron transfer during intermediate adsorption [55]. Bader-charge analysis is

employed to better explain the electronic activity of the lateral Fe–Co throughout intermediate adsorption following the ORR energetics. When $O_2$ is adsorbed, the Fe site loses electron density, and the O atoms gain charge, indicating significant electron back-donation and O—O bond activation. To stabilize the Fe–O interactions, only a fraction of charge is also added to neighboring N atoms. However, the bridge Fe–Co exhibits better electronic interaction because the two metal centers are near one another. Fe loses electrons, O atoms obtain charge after $O_2$ adsorption, and Co shows a higher amount of electron gain than in the lateral case, implying higher cooperative charge transfer. Nearby N atoms improve the Fe–O–Co interactions. Both dual-atom structures demonstrate much reduced total charge shifts via the ORR pathway ($\Sigma\Delta q$ each step) compared to the SAC ($FeN_4$ and $CoN_4$).

This suggests that the distribution of charges decreases when the electronic output splits between two metal centers. The adsorption of OOH* and O* causes significant charge swings in SAC systems, especially $FeN_4$, suggesting a greater electronic effect on a single active site. Particularly in the bridging arrangement, the dual-atom electrode exhibits the lowest ΣΔq values. Figure S14 demonstrates a comparison of the net charge-transfer growth throughout the ORR, based on Bader charge estimates, among all four systems. In comparison to their single-atom analogue, the dual-atom shows significantly fewer ΔQ variations for every reaction stage, exhibiting a more regulated transfer of charge behavior and indicating improved electrochemical stability.

In dual-atom systems, this reduced charge transfer often correlates to higher ORR consistency and reduced overpotentials. The partial density of states (PDOS) for the lateral Fe–Co configuration for PDS step (OH*) is shown in Figure 8g. The PDOS of the OH* intermediate in the lateral Fe–Co arrangement exhibits significant overlapping hybridization among the O-*2p* orbitals with the Fe-*3d* states. This significant Fe–O interaction near the Fermi level suggests that Fe serves as the dominating binding location and leads to a more stable and firmly bound OH* species. In the lateral geometry, the Co-*3d* contribution exists but is less significant, meaning that Co is not heavily involved in OH* adsorption. The bridging configuration illustrated in Figure 8h, on the other hand, demonstrates a more extensive and delocalized hybridization structure where the O-*2p* orbitals interact with both the Fe-*3d* and Co-*3d* states. In comparison to the lateral system, this shift results in a less stabilized intermediate due to weaker and more dispersed bonding to OH*. In contrast, the lateral configuration shows strong, localized Fe—O bonding that excessively stabilizes OH*, whereas the bridging arrangement distributes the interaction among Fe and Co, reducing the metal-OH* binding. This electronic difference is reflected in the ORR energetics, where the lateral dual-atom encounters a greater OH* formation barrier while the bridging dual-tom, with its weaker and more regulated hybridization, achieves more favorable OH* binding and better ORR performance.

Our research of the symmetric bridging Fe–$CoN_6$ configuration is supported by convergent experimental evidence that clearly distinguishes it from unsymmetric Fe–Co atom pairs. While direct imaging of individual bridging N atoms remains challenging in the disordered N-doped carbon support, the combined evidence from Fe/Co K-edge EXAFS (characteristic Fe–Co scattering paths), WT-EXAFS, AC-HAADF-STEM (closely spaced atomic pairs), and DFT structural optimization strongly supports the bridging Fe–$CoN_6$ configuration over purely lateral or isolated sites. Specifically, the Fe K-edge and Co K-edge FT-EXAFS spectra of $Fe_A$-$Co_A$/MWCNT-NC exhibit prominent metal–metal scattering peaks at 2.05 and 2.20 Å, respectively (Figure 2e,f), in addition to the expected M–N shells. This signature is absent in the unsymmetric Fe–Co diatomic pairs [35], which show no Fe–Co scattering and are therefore described as non-dimeric atom pairs exhibiting a seesaw-type charge polarization. In contrast, our Fe–Co scattering features closely resemble the intense, symmetric Ni–Co scattering observed in the benchmark single-atom dimer NiCo-SAD-NC [33], confirming direct metal–metal interaction in a dimeric geometry. This interpretation is further corroborated by AC-HAADF-STEM images (Figure 3e,f) that reveal numerous closely spaced atomic pairs with overlapping Fe and Co signals (blue circles), consistent with the DFT-optimized bridging model (Fe–Co distance ≈ 2.46 Å). We have added a new comparative paragraph in Section 2.2 to explicitly highlight this distinction, thereby strengthening the structural research without overstating the evidence.

DFT simulation and Bader charge distribution analysis suggest both Fe and Co atom sites display a symmetric charge redistribution based on the Bader charge calculation; however, the Fe sites in the bridging Fe–Co configuration often show a slightly larger electron reduction, indicating that it is the primary ORR active site. The charge deposition focuses primarily on the deposited oxygen species coordinated to Fe in both lateral and bridging Fe–Co dual-atom systems, indicating that ORR is mainly inclined on Fe–N sites for adsorption rather than on Co–N sites. The lowest-energy adsorption arrangements, in which Fe acts as the main electron donor in intermediate stabilization, are consistent with this observation. While Fe continues to be the principal atom site regulating charge redistribution and ORR kinetics, the comparatively uniform charge distribution across Fe and Co further shows strong electronic coupling.

## 2.6 | Effect of Dual-Atom Cathodes in ZAB's Performance

Dual-site engineering in Co, Fe-DACs/NCs@PCF-based flexible ZAB with local geometry and electronic structure of $CoN_4$//$FeN_4$ dual sites exhibits an OCV of 1.440 V and a maximum power density of 43.4 mW $cm^{-2}$, outperforming the Pt/C+$RuO_2$-benchmark ZAB (1.391 V, and 30.6 mW $cm^{-2}$) [37]. Differential charge density distribution calculation by density functional theory (DFT) would enable to confirm which atomic components among $CoN_4$//$FeN_4$ enhance electrical conductivity that facilitates charge transfer during ORR in RRDE and ZAB. A significant structural distortion with asymmetric charge distribution around $FeN_4$ and $CoN_4$ centers, which could lead to more electrons transferred from Fe and Co atoms to the carbon plane, which would optimize the adsorption/desorption of oxygen-containing intermediates, given the ORR proceeds by a 4-electron pathway involving $O_2$*, OOH*, O*, and OH* intermediate adsorption [56]. $NiN_4$ single-atomic sites with $FeN_{0.0324}$ nanoclusters within the core-shell structure of $FeN_{0.0324}$ benefit from the synergistic effect, offering maximum peak power density 180.9 mW $cm^{-2}$ for

cycling for 150 h, wherein $NiN_4$-FeN shifts the Fermi level more upward for optimized adsorption of *O [57]. Atomic engineering of Co atoms into the pyridinc-N enriched carbon nanotube encapsulated Ni nanoparticles grown on 3D electrospun carbon nanofiber nano-assemblies of the CoSANi-NCNT/CNF as an air cathode exhibits a high-power density and specific capacity for rechargeable ZABs [58]. In a synergistic effect, around the Co atoms, a great reduction of the delocalization around the metal atom is expected for the ideal environment for interaction with oxygen intermediates. The complex of Fe/Co with N atoms to form $C-N_3-Fe-Co-N_4-C$ structure with an unsymmetrical chemical and coordination structure of dual atom site, which showed a lifting effect of Fe sites on Co sites in unsymmetric structures, forms a seesaw effect to reduce the energy barrier of the decisive step of the multiphase process. In the unsymmetric model, electron orbitals are rearranged, and the electron distribution of the Co site is abnormal. The number of spin-down electrons (4.73) at Co site increases significantly, far more than the number of spin-up electrons (2.58), showing a large spin polarization. This species has very few unpaired electrons, where a weak symmetric peak corresponds to the delocalized electrons. Therefore, the attachment of the hostages inside the security wherein metal-metal bonding sometimes plays a major role. The theoretical simulation further demonstrated that the dual $Fe_A$-$Co_A$ atomic structure possesses a remarkable performance, such as peak power density, OCV, and cycling stability (Table S2, entry 1) [58].

## 2.7 | Effect of Dual-Atom Cathodes as Compared to Other Emerging ZAB Materials

Interface-confined atomic sites favor oxygen-driven surface reconstruction, which again supports atomic rearrangement, which could offer low-coordinated atomic sites for stabilizing oxygen, a key active center for ORR [59]. The desired structural modulation should be such that in a negative shift of the d-band center and effectively lowers the adsorption energy of *OH intermediates. To achieve a high ORR half-wave potential ($E_{1/2}$) of 0.86 V (vs RHE) with minimal performance loss in Co and $CeO_2$-based bifunctional electrode after a significant cycles (10 000), an excellent OER potential and a low bifunctional potential gap are needed to surpass the commercial $Pt/C+RuO_2$ as cathode in ZABs [60]. Fe-SAs/MPC, which endows abundant macropores and identical microstructural features to hard carbon, with ultra micropores walls typically comprise 1–4 layers of crumpled graphene sheets. This displays quasi-solid-state ZABs, which work stably with insignificant increase of voltage gaps for 1600 and 100 h [61]. A significant comparison of dual-atomic materials as electrodes consists of classifying dual-atom structures into three different classes such as 1) homo-diatomic, 2) hetero-diatomic, and 3) dual-atomic bridge-coupling structures. A dual single-atom P-FeCo/NC consisting of P-bridging Fe and Co bimetal atom (Fe-P-Co) on N, P-Co-doped carbon framework wherein facile adsorption/desorption of O-intermediate works for ZABs [62]. It is realized that an electron-withdrawing P atom as a bridging site customizes the dissociative ORR route as electron delocalization on P is much stronger as compared to N atom, which better tailors the electronic states of adjacent atom sites, unlike in asymmetric Co—S—Fe bonds at the heterointerface, inducing a bridge-driven multi-site synergy for promoting electron redistribution and surface polarity [63]. The adsorption energy of OH on the $FeCoN_5P$ site is more negative than that of the $FeCoN_6$ symmetric site, corresponding to higher thermodynamic stability of OH on the P bridging site. OH would tailor the adsorption-desorption properties of ORR intermediates on a $FeCoN_5P$ site, which switches the last electron transfer step ($OH{\cdot}H_2O$) from endo to exothermic, resulting in a lowest energy barrier for a $FeCoN_5P$-OH site (~0.4 eV) of the rate-determining step for ORR as compared to P-free sites such as $FeN_4$ (0.66 eV) and $FeCoN_6$ (0.99 eV). The $3dz^2$ orbital energy levels of Fe and Co atoms can selectively customize the dissociative ORR route without the formation of OOH* intermediates, circumventing the convenient OH*-OOH* scaling relations [64]. The role of interatomic distance in a dual-atom system (Cu/Ni-NC), in which theoretical calculation and advanced experiments, such as AC-HAADF-STEM, reveal that an atomic distance of Cu—Ni ~4.08 Å maximizes the synergistic interactions between two atoms for a $eCO_2RR$ and higher Faradaic efficiency ($FE_{CO}$) [65].

Besides the activity of dual-atom electrodes in general for their less revealed synergistic effects, bifunctionality of iridium nanoparticles on holey carbon via strong Ir-NHC interaction offers a 1.6-fold higher specific capacity and cycling stability for 2000 cycles, resulting from such interaction as revealed from X-ray spectroscopic analysis focused on size and electronic structure of the Ir NPs [66]. Robust ORR by radical generation on atomic pair Fe-V ($Fe_1V_1$-NC), consisting of $FeN_4$ and $VN_4$ with intersite electron interaction for boosting ORR and by avoiding the formation of ROS and offering exceptional durability [67]. Enhancing interconnected conductive pathways in Ru@TS@C results in rapid charge transfer across the 3D network for enabling enhanced reaction kinetics in ZABs, wherein Ru-mediated electron exchange with oxygen adsorbates accelerates $4e^-$ dominant oxygen reduction reaction [68]. Similarly, electronic tuning in boron atom gap-doped $Pt_3Co$ nanoparticles on carbon nanobowls (B-$Pt_3Co$/CNBs) wherein highly electronegative B atoms lead to Pt atoms to lose electrons, resulting $Pt_3Co$ weakening the bonding strength Pt—O and accelerating the protonation and desorption of O* on the surface [69].

Electrostatic spinning-in situ copolymerization-based bifunctional systems with a single-atom $FeN_x$ and $FeCoO_x$ offer high power for >580 cycles, depending on the shifts of d-band centers; however, they failed to determine the effect of carbon fibers in ZABs [70]. Providing a scaffold with cellulose nanofiber (CNF), depending on physical interweaving and strong electrostatic repulsion by the formation of hydrogen bonds for carbon aerogel with channel-oriented microstructure, with $M-N_4$ sites offering ORR activity, which results in tremendous operative stability under structural deformation, emphasizing the significance of CNF in forming aerogel [71]. Micro/nanofiber-based carbon aerogel with $Fe-N_4$ single atoms and Fe-atomic clusters (CMNCA-$Fe_{SA+AC}$) offers optimized electronic structure for ORR as a result of a biological neutral network, which is a structural biomimetic strategy with tailored single atoms that emphasizes the nanofiber-structure of the electrode [72]. N-doped CNFs host atomically dispersed metals in single and di-atomic form, wherein the nanofiber is created via electrospinning, again, where the role of nanofibers remains unrecognized [73]. A bifunctional single-atom $Co-N_5$ sites offer exceptionally high atomic utilization along with flexible carbon CNF for enhancing ZABs peak power

density and long-term cycling stability [74]. Defective CNFs with edge-located Fe-$N_4$ sites due to Zn-assisted thermal etching result in activity-enhanced ORR due to reduced Fe state; however, before defect engineering, CNFs' structure must have been investigated for their role in ORR [75]. 3D electrospun CNF nanoassemblies CoSANi-NCNT/CNF offer a multidimensional carbon skeleton, offering an ideal electronic environment for ZABs at high power density [58]. Coaxial electrospinning strategy for CNF self-supporting membrane with CoN particles and FeSA confirms the role of both on a CNF and possible proton and electron transfer mode between sites [76]. However, in spite of recent investigations on CNF-based electrospun nanofibers containing atomic and nanoparticles, exclusive structural features such as the role of non-electrospun nanofibers, multi-walled nanofibers, and hetero-diatomic sites with adjacent metal atoms without any bonding or bridging atoms on fibrous support were never addressed with sufficient evidence. The most significant scope remains in addressing the following features of the ZAB electrode with experimental evidence and theoretical support: 1) role of non-electrospun nanofiber with multi-walled structure, 2) role of Fe−Co dual atom on fibrous structure for robust ORR and ZAB performance, 3) precise comparison of Fe−Co dual atom with Fe-SA electrode for ZABs.

### 2.8 | A Close Comparison of Dual-Atom Geometry and Electronics

A close comparison of dual-atomic Fe−Co pairs for promoting kinetics of ORR and ZABs as a cathode involves the type of dual-atomic sites consisting of either bridging or lateral configuration of atom pairs, and whether consisting of symmetrical or unsymmetrical coordination geometry of atom pairs. An electron spin broken-symmetry of Fe−Co dual atomic pairs (Table S3, entry 1) for which a comparison between a symmetrical and unsymmetrical dual-atomic Fe−Co pair model was made between the free energy diagram of ORR (charging process), which showed that the Fe-site consists lower overpotential ($\mu$ = 0.33 V) as compared to Co site. This showed the Fe-site being the main active site of ORR for the symmetrical configuration of Fe−Co pair. However, for an unsymmetrical Fe−Co pair, Co sites showed lower overpotential ($\mu$ = 0.27 V) for ORR. In the symmetric model Fe−Co, more spin-up electrons than spin-down electrons is expected with almost a similar electron distribution. However, in an unsymmetrical Fe−Co pair, the d-band center moves negatively, with more electrons occupying the antibonding orbitals, resulting in weaker bond strength with oxygen intermediates, which is more conducive to the dissociation of the intermediates [35]. Fe SAs coordinated by nitrogen and Fe atomic clusters along with Co−$N_4$ moieties and CoFe NCs in Co, Fe-DACs/NCs@PCF consists of Fe-$N_4$ and Co-$N_4$ dual atoms with adjacent Fe-nanoclusters, which exhibits ORR higher onset potential of 1.09 V and a higher $E_{1/2}$ of 0.871 V. This system exhibits $Fe_5$ and $Co_2Fe_2$ clusters, introducing significant structural distortions with asymmetric charge distribution around $FeN_4$ and $CoN_4$ centers which resulting into more electrons being transferred from Fe and Co atoms to carbon planes. Herein, due to the nanoclusters' contributions in a $Co_2Fe_2$@$CoN_4$−$Fe_5$@$FeN_4$, the total density of states near the Fermi levels than those of $CoN_4$ and $FeN_4$, confirming enhanced electrical conductivity, facilitating facile charge transfer during ORR [37].

The $\varepsilon_d$ of Ni site for $NiN_4$-$FeN_4$ near the Fermi level was shifted upward, and such changes were favorable for the adsorption process of the reaction intermediates. $FeN_{0.0324}$@$NiN_4$/C enable to induce the polarization of the interfacial hydrogen bonding network in the EDL, which would affect the water dissociation kinetics. The charge redistribution between $FeN_{0.0324}$ and $NiN_4$ in the core–shell structural $FeN_{0.0324}$@$NiN_4$/C could facilitate the adsorption of *OH to accelerate the water dissociation process [57]. DOS investigation reveals the 2p-orbitals of carbon, nearby N-atoms 2p, and 3d states of Fe/Co facilitate adsorption of intermediates [77]. A NiCo-SAD-NC dimer single-atom exhibits a HER overpotential 54.7 and 61 mV at −10 mA $cm^{-2}$ in acidic and alkaline media [33]. Ni−Co dimer sites (marked by the yellow square) with coordination between Ni and Co at the atomic level, along with some isolated Ni or Co atoms with an average dimer distance of 0.241 ± 0.024 nm in the form of NiXo-$N_6$ structure. Similarly, a dual atom dimer site CuNi@GO exhibits a lowering of overpotential due to d-band electron shifting and more favored over Cu sites for OER with reach a current density of 10 mA $cm^{-2}$ with the lowest Tafel slope of 110 mV/dec for oxygen evolution reaction [1]. It is also discovered that a dual atom $Co_2N_5$ with low spin magnetic moments disrupts the conventional $\Delta G_{OOH^*}$ to $\Delta G_{OH^*}$ scaling relations, achieving optimal O* adsorption and moderated H* adsorption/desorption [9].

Therefore, it revealed that the $M_1$−$M_2$ dual-atom pair must form a suitable configuration for favorable adsorption-desorption electronics for lowering the overpotential of the electrochemical process. Table S3 and the above discussion on the geometry of the $M_1$−$M_2$ dual-atomic pair suggest that an asymmetric configuration (no symmetric bridging atoms, two metal atoms far from each other) and inclusion of nanoclusters with dual-atom sites alter the d-band electron movement by lowering the overpotential of the ORR to the maximum extent.

## 3 | Conclusion

In summary, we have assembled a ZAB cell with specific discharging capacities at 10 mA $cm^{-2}$ with the maximum power density 90 mW $cm^{-2}$ with $Fe_A$-$Co_A$/MWCNT-NC as cathode which outperforms Pt/C and FeSA950NC as revealed from discharging polarization curves and the corresponding power density. This experimental comparative analysis can be attributed to the integration of an optimized dual-atomic Fe-$N_4$/Co-$N_4$ site in $Fe_A$-$Co_A$/MWCNT-NC, consisting of a symmetric bridging configuration. Experimental and DFT simulation support further reveal that the electronic structure of the $Fe_A$−$Co_A$ dual atom site can effectively accelerate the desorption of the *OH intermediate and optimize the *OOH/*O adsorption behavior during the ORR, which forms the basis for ZABs performance. EXAFS pattern corresponding to Fe−Co scattering and AC-HAADF-STEM imaging of $Fe_A$-$Co_A$/MWCNT-NC, along with STEM mapping of elements, suggest the presence of Fe-$N_4$ and Co-$N_4$ sites in a ribbon-like nanofiber. The ZAB assembled with the $Fe_A$-$Co_A$/MWCNT-NC as an air-cathode and Zn-metal plate anode exhibited an outstanding peak power density 213 mW $cm^{-2}$. Notably, $Fe_A$-$Co_A$/MWCNT-NC as air cathode delivers at a current density of 5 mA $cm^{-2}$ remain steady until 104 h. DFT simulation reveals that the $FeN_4$ single-atom with greater

$\Sigma\Delta q$ values and restricted electron redistribution, resulting in fewer evenly distributed ORR energetics and a relatively greater overpotential, whereas Fe−Co dual-atom exhibits improved electronic cooperation, with 1) symmetric bridging arrangement, 2) most stable development of ORR intermediates and 3) least charge-transfer strain. This Fe and Co bridging site enhances O−O activation and reduces important ORR energy barriers, as confirmed by the combined PDOS and Bader-charge analyses by confirming shared and optimal charge transfer at bridging with electronic synergy. Overall, the symmetric bridging Fe−Co performs superior to the single-atom system and the lateral dual-atom configuration, along with more adsorption-desorption of intermediates of ORR on Co-$N_4$ sites as synergistic imbalance. This combined XANE-EXAFS, HAADF-STEM, and DFT simulation on $Fe_A$-$Co_A$/MWCNT-NC provides incredible insights into the underlying mode of action of dual-atomic sites for ORR and ZABs as compared to single-atom sites. These combined experimental and simulation-based findings offer insights into electron redistribution in dual-atomic sites and advance rational design for high-performance electrodes in energy storage batteries.

## Author Contributions

The manuscript was written through contributions of all authors. All authors have given approval to the final version of the manuscript. Anubha Yadav and Antra Mohini contributed equally to this work. Anubha Yadav: Manuscript writing, experiments, interpreatation, design of materials preparation, characterizaion, and electrochemical experiments. Antra Mohini: DFT simulation. Babasaheb M. Matsagar: AC HAADF STEM analysis and XRD. Norman C.-R. Chen: XANE-EXAFS spectral experiemnts. Ahin Roy: AC HAADF STEM analysis. Kevin C.-W. Wu: AC HAADF STEM analysis and XRD. Amreen Bano: Manuscript writing, interpreatation, design of experiments supervise for DFT simulation. Saikat Dutta: Manuscript writing, interpreatation, design of electrochemical experiments, direction for the preparation of samples, supervise, resource, project lead.


## Acknowledgements

S.D. wishes to acknowledge research funding support by the Science & Engineering Research Board (SERB), Department of Science & Technology, Government of India, for support through core research grant number CRG/2023/000044 (2024–2027). S.D. also wishes to thank the Department of Biotechnology, Ministry of Science & Technology, Government of India, for a DBT-Energy Bioscience-Biofuels research grant number BT/PR38594/PBD/26/795/2020 (2023–2026). S.D. thanks the UGC-DAE Consortium for Scientific Research for a project under the Collaborative Research Scheme (CRS) project grant number CRS/2022-23/01/680 (2023–2026) and the Raja Ramanna Centre for Advanced Technology, Indore Beam Line 3 and 9 for soft and hard X-ray absorption spectroscopy. The authors want to acknowledge NSRRC, Taiwan, Dr. Chan, Ting-Shan, and Dr. Pao, Chih-Wen for providing beamtimes and facilitating the SWLS-EXAFS experiments. AM and AB would like to thank TCG CREST for providing financial support, research infrastructure, and resources. The authors also gratefully acknowledge IISER Pune for providing access to the PARAM Brahma, High Performance Computing Facility, which supported the computational work presented in this study


## Conflicts of Interest

The authors declare no conflicts of interest.

## Data Availability Statement

Research data are not shared.

## References


1. S. Musa, B. M. Pirzada, S. H. Talib, et al., "Growth of Copper-nickel (Cu-Ni) Dual Atom Catalysts over Graphene Variants as Active Anodes for Clean Oxygen Generation: Integrative Experimental and Computational Validation," *Nano Energy* 125 (2024): 109479, https://doi.org/10.1016/j.nanoen.2024.109479.

2. Z. Li, X. Lu, S. Gao, et al., "Decoding the Reaction Mechanisms of $WS_2$-Confined Atomic Co Sites in Hydrogenation and Hydrogen Production Reactions," *Advanced Functional Materials* 36 (2025): 31497, https://doi.org/10.1002/adfm.202531497.

3. Z. Li, H. Liu, Y. H. Wang, et al., "Electronic Structure Modulation Induced by the Synergy of Cobalt Low-Nuclearity Clusters and Mononuclear Sites for Efficient Oxygen Electrocatalysis," *ACS Nano* 19, no. 1 (2025): 1600–1610, https://doi.org/10.1021/acsnano.4c15035.

4. M. Liu, Y. Liu, X. Zhang, et al., "Altering the Symmetry of Fe–N–C by Axial Cl-Mediation for High-Performance Zinc–Air Batteries," *Angewandte Chemie International Edition* 64, no. 26 (2025): 202504923, https://doi.org/10.1002/anie.202504923.

5. X. M. You, B. Xu, H. Zhou, et al., "Ultrahigh Bifunctional Photocatalytic $CO_2$ Reduction and $H_2$ Evolution by Synergistic Interaction of Heteroatomic Pt–Ru Dimerization Sites," *ACS Nano* 18, no. 13 (2024): 9403–9412, https://doi.org/10.1021/acsnano.3c10807.

6. L. Wang, Y. Liu, H. Wang, et al., "Oxygen-Bridged Vanadium Single-Atom Dimer Catalysts Promoting High Faradaic Efficiency of Ammonia Electrosynthesis," *ACS Nano* 17, no. 8 (2023): 7406–7416, https://doi.org/10.1021/acsnano.2c11954.

7. M. Liang, X. Shao, and H. Lee, "Recent Developments of Dual Single-Atom Catalysts for Nitrogen Reduction Reaction," *Chemistry—A European Journal* 30, no. 2 (2024): 202302843, https://doi.org/10.1002/chem.202302843.

8. T. Zhou, T. Lv, B. Xiao, et al., "Cu and Pd Dual-single-atoms Anchored Titanium Dioxide for Remarkable Photocatalytic $H_2$ Evolution Efficiency," *Chemical Engineering Journal* 478 (2023): 147372, https://doi.org/10.1016/j.cej.2023.147372.

9. X. Wang, L. Xu, C. Li, et al., "Developing a Class of Dual Atom Materials for Multifunctional Catalytic Reactions," *Nature Communications* 14, no. 1 (2023): 7210, https://doi.org/10.1038/s41467-023-42756-8.

10. N. Nwaji, G. M. Zewdie, J. Gwak, et al., "Dimeric Ni Co Single-atom Anchored on Ultrathin N-doped 2D Molybdenum Carbide Boosted Performance in Solid-state Supercapacitor," *Journal of Energy Storage* 83 (2024): 110671, https://doi.org/10.1016/j.est.2024.110671.

11. M. Liu, N. Li, S. Cao, et al., "A "Pre-Constrained Metal Twins" Strategy to Prepare Efficient Dual-Metal-Atom Catalysts for Cooperative Oxygen Electrocatalysis," *Advanced Materials* 34, no. 7 (2022): 2107421, https://doi.org/10.1002/adma.202107421.

12. X. Li, C. Qian, Y. Tian, N. Yao, Y. Duan, and Z. Huang, "Pt-Ru Bimetallic Nanoclusters with Super Peroxidase-Like Activity for Ultra-Sensitive Lateral Flow Immunoassay," *Chemical Engineering Journal* 457 (2023): 141324, https://doi.org/10.1016/j.cej.2023.141324.

13. V. Giulimondi, S. K. Kaiser, A. J. Martin, et al., "Controlled Formation of Dimers and Spatially Isolated Atoms in Bimetallic Au-Ru Catalysts via Carbon-Host Functionalization," *Small* 18, no. 15 (2022): 2200224, https://doi.org/10.1002/smll.202200224.

14. T. Tang, Z. Wang, and J. Guan, "Structural Optimization of Carbon-based Diatomic Catalysts towards Advanced Electrocatalysis," *Coordination Chemistry Reviews* 492 (2023): 215288, https://doi.org/10.1016/j.ccr.2023.215288.

15. L. Zhang, R. Si, H. Liu, et al., "Atomic Layer Deposited Pt-Ru Dual-Metal Dimers and Identifying Their Active Sites for Hydrogen Evolution

Reaction," *Nature Communications* 10, no. 1 (2019): 4936, https://doi.org/10.1038/s41467-019-12887-y.

16. X. Zhu, Q. Guo, Y. Sun, et al., "Optimising Surface D Charge of AuPd Nanoalloy Catalysts for Enhanced Catalytic Activity," *Nature Communications* 10, no. 1 (2019): 1428, https://doi.org/10.1038/s41467-019-09421-5.

17. N. Zhang, Y. Si, X. Chen, X. Wang, and J. Yao, "Bimetallic Synergy in Single-Atom Alloy Nanocatalysts for $CO_2$ Reduction to Ethylene," *ACS Applied Nano Materials* 6, no. 4 (2023): 2394–2402, https://doi.org/10.1021/acsanm.2c04474.

18. L. Wu, Y. Chen, C. Shao, L. Wang, and B. Li, "Engineering Synergetic Fe-Co Atomic Pairs Anchored on Porous Carbon for Enhanced Oxygen Reduction Reaction," *Advanced Functional Materials* 34, no. 48 (2024): 2408257, https://doi.org/10.1002/adfm.202408257.

19. S. Qiu, H. Wan, Y. Yao, et al., "Atomically Dispersed Zr-N Moieties Modulate Fe Coordination for Robust Oxygen Reduction Electrocatalysis," *Advanced Science* 12, no. 47 (2025): 12381, https://doi.org/10.1002/advs.202512381.

20. X. Ao, L. Li, S. Y. Yun, et al., "Highly Accessible Dual-metal Atomic Pairs for Enhancing Oxygen Redox Reaction in Zinc−Air Batteries," *Nano Energy* 118 (2023): 108952, https://doi.org/10.1016/j.nanoen.2023.108952.

21. G. Dey, R. Jana, S. Saifi, et al., "Dual Single-Atomic Co–Mn Sites in Metal–Organic-Framework-Derived N-Doped Nanoporous Carbon for Electrochemical Oxygen Reduction," *ACS Nano* 17, no. 19 (2023): 19155–19167, https://doi.org/10.1021/acsnano.3c05379.

22. Y. Wang, S. Pan, Z. Lu, et al., "Boosting Bifunctional Oxygen Electrocatalysis with Atomically Dispersed Fe and Co Dual-Metal Sites for Flexible Zinc-Air Batteries," *Chemical Engineering Science* 282 (2023): 119304, https://doi.org/10.1016/j.ces.2023.119304.

23. W. Zhang, M. Nie, and C. He, "Machine Learning-Driven Band Alignment Strategy for Screening 1T-TMDs-Based Z-Scheme Heterostructures toward Efficient Photocatalytic Water Splitting," *Small* 21, no. 31 (2025): 2504095, https://doi.org/10.1002/smll.202504095.

24. C. He, L. Wang, and W. Zhang, "Mechanistic Insights into Coordination Engineering of Dual-Atom Catalysts on B-N-doped Graphene toward Efficient Nitrogen Reduction," *Applied Surface Science* 726 (2026): 165867, https://doi.org/10.1016/j.apsusc.2026.165867.

25. W. Zhang, S. Ruan, Z. Jiang, H. Yan, and C. He, "Unraveling the Synergistic Mechanism of Trimetallic Ni–Fe–Cu in Nanoflower-layered Electrocatalysts for Enhanced Oxygen Evolution Reaction," *Surfaces and Interfaces* 82 (2026): 108462, https://doi.org/10.1016/j.surfin.2026.108462.

26. S. Ji, Y. H. Wang, H. Liu, et al., "Site-Specific Synergy by Heteronuclear Microenvironment Atomic Editing for Oxygen Reduction Reaction," *Nature Communications* 16, no. 1 (2025): 11691, https://doi.org/10.1038/s41467-025-66841-2.

27. A. Yadav, N. Hiremath, B. Saini, et al., "Coordinately Unsaturated Single Fe-atoms with N Vacancies and Enhanced $sp^3$ Carbon Defects in Fe–N($sp^2$)–C Structural Units for Suppression of Cancer Cell Metabolism and Electrochemical Oxygen Evolution," *Nanoscale* 16, no. 46 (2024): 21416–21430, https://doi.org/10.1039/D4NR02553A.

28. A. Pramanik, S. Suriyakumar, T. Pieshkov, et al., "Graphite Cone/Disc Anodes as Alternative to Hard Carbons for Na/K-Ion Batteries," *Advanced Functional Materials* 35, no. 37 (2025): 2505848, https://doi.org/10.1002/adfm.202505848.

29. X. Cui, L. Gao, S. Lei, et al., "Simultaneously Crafting Single-Atomic Fe Sites and Graphitic Layer-Wrapped $Fe_3$ C Nanoparticles Encapsulated within Mesoporous Carbon Tubes for Oxygen Reduction," *Advanced Functional Materials* 31, no. 10 (2020): 2009197, https://doi.org/10.1002/adfm.202009197.

30. Z. Tang, R. Zhang, H. Wang, et al., "Revealing the Closed Pore Formation of Waste Wood-Derived Hard Carbon for Advanced Sodium-Ion Battery," *Nature Communications* 14, no. 1 (2023): 6024, https://doi.org/10.1038/s41467-023-39637-5.

31. X. Zhu, D. Zhang, C. J. Chen, et al., "Harnessing the Interplay of Fe–Ni Atom Pairs Embedded in Nitrogen-Doped Carbon for Bifunctional Oxygen Electrocatalysis," *Nano Energy* 71 (2020): 104597, https://doi.org/10.1016/j.nanoen.2020.104597.

32. H. B. Yang, S. F. Hung, S. Liu, et al., "Atomically Dispersed Ni(i) as the Active Site for Electrochemical $CO_2$ Reduction," *Nature Energy* 3, no. 2 (2018): 140–147, https://doi.org/10.1038/s41560-017-0078-8.

33. A. Kumar, V. Q. Bui, J. Lee, et al., "Moving beyond Bimetallic-Alloy to Single-Atom Dimer Atomic-Interface for all-pH Hydrogen Evolution," *Nature Communications* 12, no. 1 (2021): 6766, https://doi.org/10.1038/s41467-021-27145-3.

34. W. Ren, X. Tan, W. Yang, et al., "Isolated Diatomic Ni-Fe Metal–Nitrogen Sites for Synergistic Electroreduction of $CO_2$," *Angewandte Chemie International Edition* 58, no. 21 (2019): 6972–6976, https://doi.org/10.1002/anie.201901575.

35. X. Li, J. Qin, Q. Lin, et al., "Electron Spin Broken-Symmetry of Fe–Co Diatomic Pairs to Promote Kinetics of Bifunctional Oxygen Electrocatalysis for Zinc–Air Batteries," *Advanced Science* 11, no. 35 (2024): 2401187, https://doi.org/10.1002/advs.202401187.

36. Z. Lu, B. Wang, Y. Hu, et al., "An Isolated Zinc–Cobalt Atomic Pair for Highly Active and Durable Oxygen Reduction," *Angewandte Chemie International Edition* 58, no. 9 (2019): 2622–2626, https://doi.org/10.1002/anie.201810175.

37. Z. Lu, Z. Wang, Z. Yang, et al., "Engineering $CoN_4$ and $FeN_4$ Dual Sites with Adjacent Nanoclusters on Flexible Porous Carbon Fibers for Enhanced Electrocatalytic Oxygen Reduction and Evolution," *Advanced Functional Materials* 35, no. 16 (2024): 2418489, https://doi.org/10.1002/adfm.202418489.

38. B. Wang, J. Tang, X. Zhang, et al., "Nitrogen Doped Porous Carbon Polyhedral Supported Fe and Ni Dual-Metal Single-Atomic Catalysts: Template-free and Metal Ligand-free Sysnthesis with Microwave-assistance and D-band Center Modulating for Boosted ORR Catalysis in Zinc-air Batteries," *Chemical Engineering Journal* 437 (2022): 135295, https://doi.org/10.1016/j.cej.2022.135295.

39. R. Wu, J. Zuo, C. Fu, et al., "Enhancing Rechargeable Zinc-Air Batteries with Atomically Dispersed Zinc Iron Cobalt Planar Sites on Porous Nitrogen-Doped Carbon," *ACS Nano* 19, no. 21 (2025): 20215–20224, https://doi.org/10.1021/acsnano.5c05961.

40. S. Xi, P. Zhao, W. Zhang, and C. He, "Machine Learning-Accelerated Specific Surface Prediction Strategy in Janus-Based Z-Scheme Heterostructures for Efficient Photocatalytic Water Splitting," *Small* 22, no. 4 (2026): 09069, https://doi.org/10.1002/smll.202509069.

41. T. Li, B. Liu, H. Guo, et al., "Enhanced Bifunctional Oxygen Electrocatalysis by Synergistic Active Heterostructure Design," *Advanced Energy Materials* 15, no. 35 (2025): 2502493, https://doi.org/10.1002/aenm.202502493.

42. H. Wang, R. T. Gao, N. T. Nguyen, et al., "Superhydrophilic CoFe Dispersion of Hydrogel Electrocatalysts for Quasi-Solid-State Photoelectrochemical Water Splitting," *ACS Nano* 17, no. 21 (2023): 22071–22081, https://doi.org/10.1021/acsnano.3c08861.

43. M. Xiao, Z. Xing, Z. Jin, et al., "Preferentially Engineering $FeN_4$ Edge Sites onto Graphitic Nanosheets for Highly Active and Durable Oxygen Electrocatalysis in Rechargeable Zn–Air Batteries," *Advanced Materials* 32, no. 49 (2020): 2004900, https://doi.org/10.1002/adma.202004900.

44. G. Zhu, H. Yang, Y. Jiang, et al., "Modulating the Electronic Structure of FeCo Nanoparticles in N-Doped Mesoporous Carbon for Efficient Oxygen Reduction Reaction," *Advanced Science* 9, no. 15 (2022): 2200394, https://doi.org/10.1002/advs.202200394.

45. J. Zhao, C. Fu, K. Ye, et al., "Manipulating the Oxygen Reduction Reaction Pathway on Pt-Coordinated Motifs," *Nature Communications* 13, no. 1 (2022): 685, https://doi.org/10.1038/s41467-022-28346-0.

46. L. Zhao, Y. Zhang, L. B. Huang, et al., "Cascade Anchoring Strategy for General Mass Production of High-loading Single-Atomic Metal-Nitrogen

Catalysts," *Nature Communications* 10, no. 1 (2019): 1278, https://doi.org/10.1038/s41467-019-09290-y.

47. Y. Yan, S. Liang, X. Wang, et al., "Robust Wrinkled $MoS_2$ /N-C Bifunctional Electrocatalysts Interfaced with Single Fe Atoms for Wearable Zinc-Air Batteries," *Proceedings of the National Academy of Sciences* 118, no. 40 (2021): 2110036118, https://doi.org/10.1073/pnas.2110036118.

48. Q. Wang, Q. Feng, Y. Lei, et al., "Quasi-solid-state Zn-air Batteries with an Atomically Dispersed Cobalt Electrocatalyst and Organohydrogel Electrolyte," *Nature Communications* 13, no. 1 (2022): 3689, https://doi.org/10.1038/s41467-022-31383-4.

49. K. Tang, H. Hu, Y. Xiong, et al., "Hydrophobization Engineering of the Air–Cathode Catalyst for Improved Oxygen Diffusion towards Efficient Zinc–Air Batteries," *Angewandte Chemie International Edition* 61, no. 24 (2022): 202202671, https://doi.org/10.1002/anie.202202671.

50. Z. Liu, T. He, K. Liu, W. Chen, and Y. Tang, "Structural, Electronic and Catalytic Performances of Single-Atom Fe Stabilized by Divacancy-Nitrogen-Doped Graphene," *RSC Advances* 7, no. 13 (2017): 7920–7928, https://doi.org/10.1039/c6ra28387j.

51. Y. He, S. Hwang, D. A. Cullen, et al., "Highly Active Atomically Dispersed $CoN_4$ Fuel Cell Cathode Catalysts Derived from Surfactant-Assisted MOFs: Carbon-Shell Confinement Strategy," *Energy & Environmental Science* 12, no. 1 (2019): 250–260, https://doi.org/10.1039/c8ee02694g.

52. R. K. Raju, "Electrocatalytic Reduction of Nitrogen to Ammonia on Metal Nanoclusters: Insights and Trends from D- and p-block Metals," *Physical Chemistry Chemical Physics* 27, no. 15 (2025): 7773–7796, https://doi.org/10.1039/d5cp00046g.

53. L. Li, X. Wu, Q. Du, N. Bai, and Y. Wen, "Boosting the Oxygen Reduction Reaction Activity of Dual-Atom Catalysts on N-Doped Graphene by Regulating the N Coordination Environment," *Physical Chemistry Chemical Physics* 26, no. 1 (2023): 628–634, https://doi.org/10.1039/d3cp04831d.

54. Q. Zhou, W. Xue, X. Cui, et al., "Oxygen-bridging Fe, Co Dual-metal Dimers Boost Reversible Oxygen Electrocatalysis for Rechargeable Zn–Air Batteries," *Proceedings of the National Academy of Sciences* 121, no. 30 (2024): 2404013121, https://doi.org/10.1073/pnas.2404013121.

55. W. Zhang, S. Yi, Y. Yu, et al., "Fe-based Dual-atom Catalysts for the Oxygen Reduction Reaction," *Journal of Materials Chemistry A* 12, no. 1 (2024): 87–112, https://doi.org/10.1039/d3ta05147a.

56. S. Das, A. Pathak, U. Phadikar, et al., "Harnessing the Trade-off between CoFe/$Fe_3$ C Interfacial Junction with Unparalleled Potential Gap of 0.58 V for Reversible Oxygen Electrocatalysis: Application toward Liquid and Solid-State Zn-Air Batteries," *Advanced Functional Materials* 34, no. 44 (2024): 2407078, https://doi.org/10.1002/adfm.202407078.

57. Q. Liu, J. Chen, L. Cao, et al., "Electronic Communication between Single Atomic Nickel and Iron-Nitrogen Species Promote the Bifunctional Oxygen Evolution and Reduction for Efficient Rechargeable Zinc-Air Battery," *Advanced Functional Materials* 35, no. 25 (2025): 2424597, https://doi.org/10.1002/adfm.202424597.

58. M. B. Poudel, M. P. Balanay, P. C. Lohani, K. Sekar, and D. J. Yoo, "Atomic Engineering of 3D Self-Supported Bifunctional Oxygen Electrodes for Rechargeable Zinc-Air Batteries and Fuel Cell Applications," *Advanced Energy Materials* 14, no. 30 (2024): 2400347, https://doi.org/10.1002/aenm.202400347.

59. Z. Li, W. Tian, K. Hu, et al., "Oxygen-Driven Reconstruction Activates Quasi-Single Pd Sites in Hollow PdAg Nanotubes for Zinc–Air and Fuel Cells," *Advanced Science* 12, no. 43 (2025): 09329, https://doi.org/10.1002/advs.202509329.

60. L. Xu, Z. Mao, J. Liu, et al., "Carbon-Encapsulated $CeO_2$-Co Heterostructure via Tight Coupling Enables Corrosion-Resistant Bifunctional Catalysis in Zinc-Air Battery," *Advanced Energy Materials* 15, no. 34 (2025): 2501790, https://doi.org/10.1002/aenm.202501790.

61. H. Liu, P. Li, K. Fan, et al., "Microporous Hard Carbon Support Provokes Exceptional Performance of Single Atom Electrocatalysts for Advanced Air Cathodes," *Angewandte Chemie International Edition* 64, no. 23 (2025): 202501307, https://doi.org/10.1002/anie.202501307.

62. N. Wang, R. Mei, L. Chen, et al., "P-Bridging Asymmetry Diatomic Catalysts Sites Drive Efficient Bifunctional Oxygen Electrocatalysis for Zinc-Air Batteries," *Small* 20, no. 32 (2024): 2400327, https://doi.org/10.1002/smll.202400327.

63. L. Zhao, Y. Yang, K. Ding, et al., "Advanced Oxygen Electrocatalysis Driven by Asymmetric Interfacial Sulfur Bridge Bonding," *Advanced Energy Materials* 15, no. 43 (2025): 03189, https://doi.org/10.1002/aenm.202503189.

64. Y. Zeng, X. Wang, W. Qi, et al., "Aligned D-orbital Energy Level of Dual-atom Sites Catalysts for Oxygen Reduction Reaction in Anion Exchange Membrane Fuel Cells," *Nature Communications* 16, no. 1 (2025): 8111, https://doi.org/10.1038/s41467-025-63322-4.

65. J. Ma, W. Lee, J. H. Kim, et al., "Leveraging the Intermetal Distance in Dual-Atom Catalysts: Revealing Optimized Synergistic Interactions for $CO_2$ Electroreduction," *ACS Nano* 19, no. 19 (2025): 18698–18707, https://doi.org/10.1021/acsnano.5c03160.

66. H. You, Y. Xu, T. Shao, et al., "Enhanced Bifunctional Catalysis of Iridium Nanoparticles on Nitrogen-Doped Holey Carbon via Strong Metal–Support Interaction for Rechargeable Zinc–Air Batteries," *Angewandte Chemie International Edition* 64, no. 44 (2025): 202514873, https://doi.org/10.1002/anie.202514873.

67. L. Ran, Y. Zhang, W. Tong, et al., "Circumventing Radical Generation on Fe–V Atomic Pair Catalyst for Robust Oxygen Reduction and Zinc–Air Batteries," *Angewandte Chemie International Edition* 64, no. 45 (2025): 202514542, https://doi.org/10.1002/anie.202514542.

68. S. Liang, L. N. Song, X. X. Wang, et al., "Efficient Carrier Separation via Ru@TS@C Zeolite: Enabling Photo-Cathodes for High-Efficiency Photo-Assisted Metal−Air Batteries," *Angewandte Chemie International Edition* 64, no. 44 (2025): 202512477, https://doi.org/10.1002/anie.202512477.

69. G. R. Xu, X. Zhou, Y. Miao, et al., "Electron Synergism in Boron Interstitial Doping Ordered $Pt_3Co$ Nanoparticles Enhances the Protonation Process: Application to Efficient Oxygen Reduction in Zinc-Air Batteries," *Advanced Energy Materials* 15, no. 37 (2025): 03590, https://doi.org/10.1002/aenm.202503590.

70. K. Wei, F. Yang, Y. Sun, et al., "Tailoring Oxygen Electrocatalytic Performance via Construction of Iron-Cobalt Oxides and $FeN_4$ Sites on Hierarchical Carbon Fibers for Efficient Zinc–Air Batteries," *Advanced Functional Materials* 35, no. 32 (2025): 2422039, https://doi.org/10.1002/adfm.202422039.

71. Z. Chen, L. Zhong, Z. Chen, et al., "Reconstructed Wood Carbon Aerogel with Single-Atom Sites for Flexible Zn–Air Batteries," *ACS Nano* 19, no. 26 (2025): 23859–23868, https://doi.org/10.1021/acsnano.5c04945.

72. J. Sun, M. Shen, A. J. Chang, et al., "Biological Neural Network-Inspired Micro/Nano-Fibrous Carbon Aerogel for Coupling Fe Atomic Clusters with Fe-$N_4$ Single Atoms to Enhance Oxygen Reduction Reaction," *Small* 21, no. 15 (2025): 2500419, https://doi.org/10.1002/smll.202500419.

73. H. Zhao, B. Song, H. Li, et al., "Controllable Microwave Heating for Energy-Efficient and Universal Synthesis of Atomically Dispersed Metals on Nitrogen-Doped Carbon Nanofibers," *Small* 21, no. 4 (2025): 2407700, https://doi.org/10.1002/smll.202407700.

74. Q. Luo, K. Wang, Q. Zhang, et al., "Tailoring Single-Atom Coordination Environments in Carbon Nanofibers via Flash Heating for Highly Efficient Bifunctional Oxygen Electrocatalysis," *Angewandte Chemie International Edition* 64, no. 1 (2025): 202413369, https://doi.org/10.1002/anie.202413369.

75. R. Pang, H. Xia, X. Dong, Q. Zeng, J. Li, and E. Wang, "Zinc Assisted Thermal Etching for Rich Edge-Located Fe-$N_4$ Active Sites in Defective Carbon Nanofiber for Activity Enhancement of Oxygen Electroreduction," *Advanced Science* 11, no. 39 (2024): 2407294, https://doi.org/10.1002/advs.202407294.

76. X. Zhang, P. Yu, G. Xing, et al., "Iron Single Atoms-Assisted Cobalt Nitride Nanoparticles to Strengthen the Cycle Life of Rechargeable Zn–Air Battery," *Small* 18, no. 51 (2022): 2205228, https://doi.org/10.1002/smll.202205228.

77. C. Y. Su, H. Cheng, W. Li, et al., "Atomic Modulation of FeCo–Nitrogen–Carbon Bifunctional Oxygen Electrodes for Rechargeable and Flexible All-Solid-State Zinc–Air Battery," *Advanced Energy Materials* 7, no. 13 (2017): 1602420, https://doi.org/10.1002/aenm.201602420.

## Supporting Information

Additional supporting information can be found online in the Supporting Information section.

**Supporting File**: smll74296-sup-0001-SuppMat.docx.